

# East Asia orogenesis restricted oceanic circulation between Paleo-Tethys and Panthalassa before the Permian mass extinction

Lei Zhao<sup>1</sup>, Hu Tang<sup>1</sup>, Ross N Mitchell<sup>1</sup>, Qiu-Li Li<sup>1</sup>, Xiwen Zhou<sup>2</sup>, and Mingguo Zhai<sup>3</sup>

<sup>1</sup>Institute of Geology and Geophysics, Chinese Academy of Sciences

<sup>2</sup>Institute of Geology, Chinese Academy of Geological Sciences

<sup>3</sup>Institute of Geology and Geophysics, Chinese Academy of Sciences

December 22, 2022

## Abstract

The Paleo-Tethys and Panthalassa are two major oceans that witnessed the end-Permian mass extinction, and they have been suggested to have distinct compositions, with the Paleo-Tethys Ocean euxinic, and the much larger Panthalassa Ocean being largely ventilated. Distinctions of these two once-connected oceans imply that interactions between them must have been restricted shortly before the end-Permian extinction. However, detailed geological processes for the disconnection between them along the eastern Paleo-Tethys Ocean due to the collision of North and South China, are still unclear. Previous geochronological studies on eclogite facies rocks in the Dabie–Sulu orogenic belt, which are the metamorphic products of the collision between North and South China, have yielded mainly Triassic metamorphic ages. Nonetheless, new Permian metamorphic ages are identified from southeastern North China, northern Dabie, and the Permo–Triassic intracontinental orogen of South China, which may collectively closely associate this major tectonic event with the end-Permian extinction. New age dating results, as well as a synthesis of recent studies on metamorphic rocks, show that the onset of the collisional orogenesis dates back to the Middle Permian (270–252 Ma). We thereby provide a new tectonic model for the major continents of East Asia, in which the initial collision between North and South China during the Middle Permian critically isolated the Paleo-Tethys Ocean from the Panthalassa Ocean, facilitating the oceanographic transition of the once fossiliferous Paleo-Tethys from a life-giving nutrient-rich ocean into a euxinic death trap, thereby serving as prelude to the end-Permian extinction.

## Hosted file

951352\_0\_art\_file\_10503531\_rmdgc8.docx available at <https://authorea.com/users/568963/articles/614587-east-asia-orogenesis-restricted-oceanic-circulation-between-paleo-tethys-and-panthalassa-before-the-permian-mass-extinction>

## Hosted file

951352\_0\_supp\_10503541\_rmdgc9.docx available at <https://authorea.com/users/568963/articles/614587-east-asia-orogenesis-restricted-oceanic-circulation-between-paleo-tethys-and-panthalassa-before-the-permian-mass-extinction>

## Hosted file

951352\_0\_supp\_10503543\_rmdgc9.docx available at <https://authorea.com/users/568963/articles/614587-east-asia-orogenesis-restricted-oceanic-circulation-between-paleo-tethys-and-panthalassa-before-the-permian-mass-extinction>

1  
2 **East Asia orogenesis restricted oceanic circulation between Paleo-Tethys and**  
3 **Panthalassa before the Permian mass extinction**

4 **L. Zhao<sup>1</sup>, H. Tang<sup>1</sup>, R.N. Mitchell<sup>1</sup>, Q.L. Li<sup>1</sup>, X.W. Zhou<sup>2</sup>, M.G. Zhai<sup>1</sup>**

5 <sup>1</sup>State Key Laboratory of Lithospheric Evolution, Institute of Geology and Geophysics, Chinese  
6 Academy of Sciences, 100029, Beijing, China.

7 <sup>2</sup>Institute of Geology, Chinese Academy of Geological Sciences, 100037, Beijing, China.

8 Corresponding authors: L. Zhao ([zhaolei@mail.iggcas.ac.cn](mailto:zhaolei@mail.iggcas.ac.cn)), R.N. Mitchell  
9 ([ross.mitchell@mail.iggcas.ac.cn](mailto:ross.mitchell@mail.iggcas.ac.cn)), Q.L. Li ([liquli@mail.iggcas.ac.cn](mailto:liquli@mail.iggcas.ac.cn)), M.G. Zhai  
10 ([mgzhai@mail.iggcas.ac.cn](mailto:mgzhai@mail.iggcas.ac.cn))

11 **Key Points:**

- 12 • Continental collision between the North and South China resulted in pervasive  
13 metamorphism in East Asia.
- 14 • New geochronological results reveal the onset of the collisional event during Permian,  
15 rather than Triassic as previously suggested.
- 16 • The orogenesis closed the seaway connecting Paleo-Tethys and Panthalassa before the  
17 Permian mass extinction.  
18

## 19 **Abstract**

20 The Paleo-Tethys and Panthalassa are two major oceans that witnessed the end-Permian mass  
21 extinction, and they have been suggested to have distinct compositions, with the Paleo-Tethys  
22 Ocean euxinic, and the much larger Panthalassa Ocean being largely ventilated. Distinctions of  
23 these two once-connected oceans imply that interactions between them must have been restricted  
24 shortly before the end-Permian extinction. However, detailed geological processes for the  
25 disconnection between them along the eastern Paleo-Tethys Ocean due to the collision of North  
26 and South China, are still unclear. Previous geochronological studies on eclogite facies rocks in  
27 the Dabie–Sulu orogenic belt, which are the metamorphic products of the collision between  
28 North and South China, have yielded mainly Triassic metamorphic ages. Nonetheless, new  
29 Permian metamorphic ages are identified from southeastern North China, northern Dabie, and  
30 the Permo–Triassic intracontinental orogen of South China, which may collectively closely  
31 associate this major tectonic event with the end-Permian extinction. New age dating results, as  
32 well as a synthesis of recent studies on metamorphic rocks, show that the onset of the collisional  
33 orogenesis dates back to the Middle Permian (270–252 Ma). We thereby provide a new tectonic  
34 model for the major continents of East Asia, in which the initial collision between North and  
35 South China during the Middle Permian critically isolated the Paleo-Tethys Ocean from the  
36 Panthalassa Ocean, facilitating the oceanographic transition of the once fossiliferous Paleo-  
37 Tethys from a life-giving nutrient-rich ocean into a euxinic death trap, thereby serving as prelude  
38 to the end-Permian extinction.

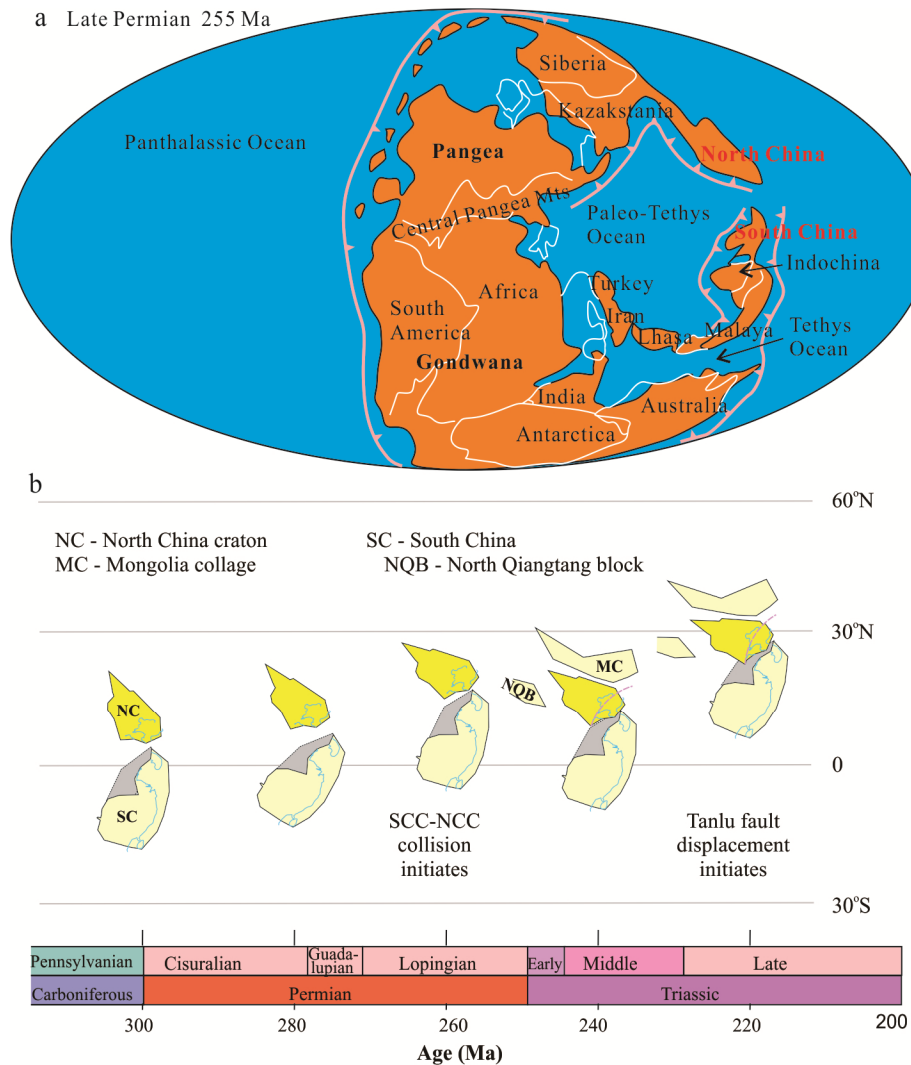
## 39 **Plain Language Summary**

40 Earth's surface processes and environmental changes are strongly influenced by its deep  
41 geodynamics and the relations between the Siberian Traps and the end-Permian mass extinction  
42 is a good example. In addition to such a final trigger, the preconditioning of a vulnerable  
43 palaeoenvironment is being increasingly acknowledged as a critical aspect for understanding  
44 mass extinctions. In recent years, studies indicate that unlike the euxinic Paleo-Tethys Ocean, the  
45 much larger Panthalassa (a.k.a., paleo-Pacific) Ocean remained largely ventilated and provided  
46 potential refugia for marine taxa during the mass extinction. However, previous  
47 geochronological studies on eclogite facies rocks in the Dabie–Sulu orogenic belt, which are the  
48 metamorphic products of the collision between North and South China, have yielded mainly  
49 Triassic metamorphic ages postdating the Permian mass extinction. This study targeted the rocks  
50 from North China, northern Dabie orogen, and South China that escaped deep subduction. They  
51 all yield Permian metamorphic ages (270–252 Ma), which collectively indicate Permian  
52 continental collision between North and South China. This fundamental geological boundary  
53 condition would have critically isolated the Paleo-Tethys Ocean from the Panthalassa Ocean, and  
54 therefore, the poorly mixed Paleo-Tethys Ocean gradually became a dead sea, thereby  
55 preconditioning and facilitating the end-Permian biospheric crisis in the region.

## 56 **1 Introduction**

57 The biosphere experienced a devastating blow during the end-Permian, when more than 81%  
58 of marine species and ~89% of terrestrial species died out (Erwin et al., 2002; Fan et al., 2020;  
59 Viglietti et al., 2021). The Siberian Traps large igneous province has long been suggested to be  
60 the primary cause of the Permian mass extinction and related environmental stress (Burgess and

61 [Bowring, 2015; Erwin, 1990](#)). Additionally, other sources of volcanic outgassing around the  
 62 world at that time, particularly the prolific magmatic arc of the Australian Tasminides, also  
 63 contributed to the overall volcanic-input aspect of the variegated kill mechanism ([Chapman et  
 64 al., 2022](#)). Global oceanic anoxia and ocean acidification have also been proposed to have causal  
 65 relations with the Permian extinction ([Clarkson et al., 2015; Isozaki, 1997; Shen et al., 2011](#)).  
 66 However, global oceanic anoxia was challenged by several studies, which pointed out that the  
 67 deep Panthalassa Ocean remained ventilated even during the expansion of the oxygen minimum  
 68 zone ([Algeo et al., 2011; Winguth and Winguth, 2012](#)). Uncertainties also exist about the ability  
 69 of the Siberian Traps and other sources of magmatism to have emitted enough toxic volatiles to  
 70 sufficiently trigger the global climate and environmental changes, which in turn, resulted in the  
 71 end-Permian mass extinction ([Davydov and Karasev, 2021; Zhang et al., 2021b](#)).



72

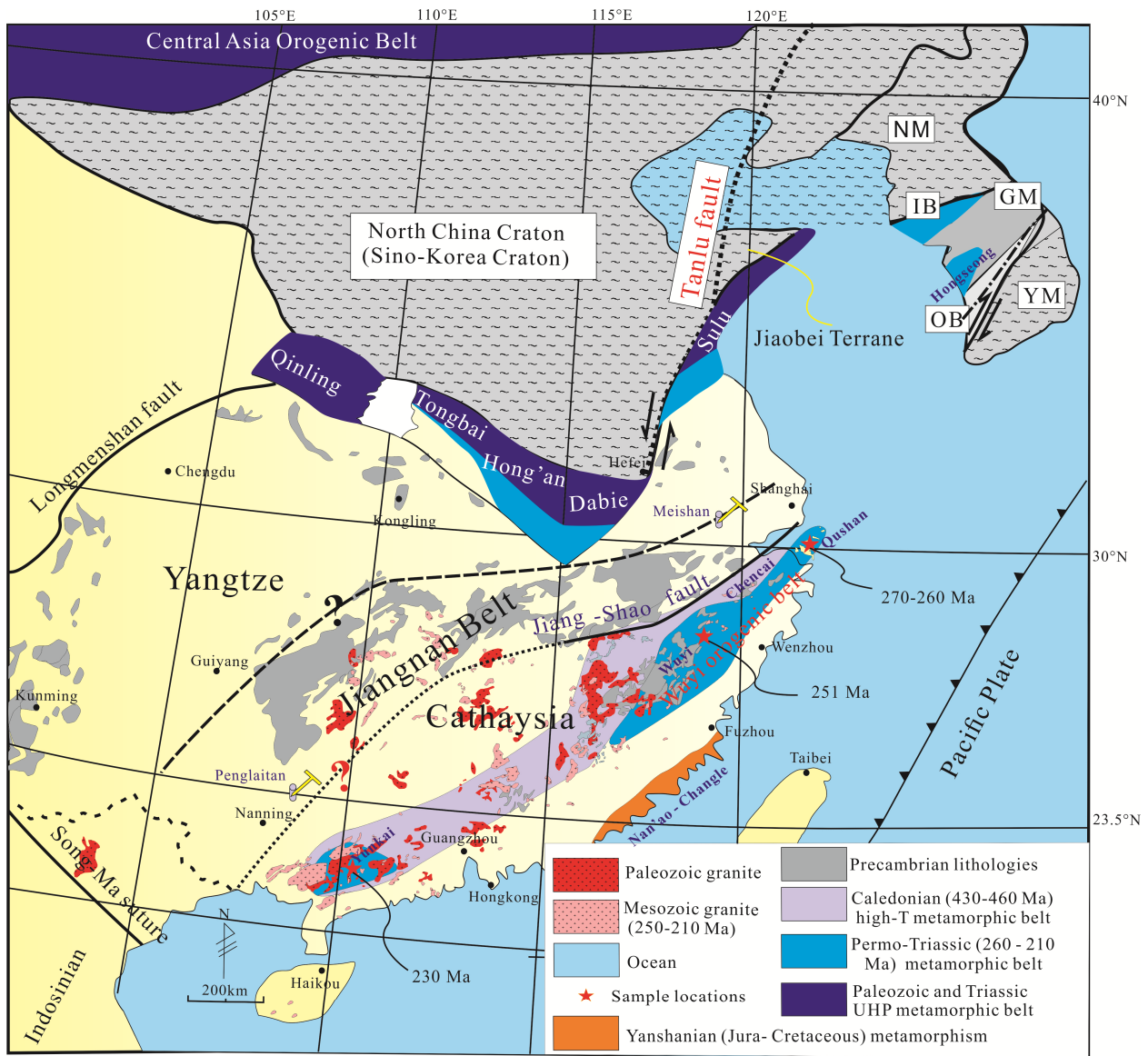
73 **Fig. 1.** Competing paleogeographic models of North and South China. (a) Early Triassic global  
 74 paleogeography ([Scotese, 1997](#)). Note large gulf between North and South China. (b)  
 75 Alternative interpretation of an earlier amalgamation of North and South China in the latest  
 76 Permian ([Huang et al., 2018](#)).

77 Unlike the Panthalassa Ocean that occupied almost half of Earth's surface, the Paleo-Tethys  
78 Ocean was relatively small, comprising only 10–15% of the area of the global oceans, and was  
79 largely euxinic (Fig. 1a) (Algeo et al., 2008, 2011; Cao et al., 2009). Furthermore, almost all the  
80 type-localities of the stratigraphic sections preserving the paleontological record of the end-  
81 Permian extinction occur in the Paleo-Tethys tectonic realm (Şengör and Atayman, 2009), a  
82 feature which might be intrinsic to its euxinic condition. Previous studies reveal that the Paleo-  
83 Tethys Ocean was a nutrient trap that also exhibited features of a stagnant ocean while the  
84 Panthalassa Ocean underwent only limited redox changes and provided potential refugia for  
85 marine taxa that survived into the Triassic (Algeo et al., 2010; Algeo and Twitchett, 2010). The  
86 different features of the two late Paleozoic oceanic realms strongly suggest that oceanic  
87 circulation between them might have become severely restricted at some point (Şengör and  
88 Atayman, 2009). Due to the amalgamation of different continental blocks with Pangea before  
89 end-Permian, the Panthalassa and the Paleo-Tethys oceans were already disconnected along the  
90 northern, southern, and western margins of the Paleo-Tethys Ocean prior to the Middle Permian  
91 (Fig. 1a) (Carter et al., 2001; Metcalfe, 2006; Stampfli et al., 2013; Wu et al., 2020). Meanwhile,  
92 most paleogeographic models depict the eastern margin of the Paleo-Tethys Ocean as still being  
93 connected to the larger Panthalassa Ocean at the time of the extinction, and even well into the  
94 Triassic (Fig. 1a; Scotese, 1997). Therefore, the role that the eastern margin of the Paleo-Tethys  
95 Ocean played in oceanic circulation at this critical time is still unclear, mainly due to the  
96 ambiguous tectonic relationship between the North and South China cratons/blocks (hereafter  
97 referred to simply as North China and South China).

98 The final collision between these two continental blocks along the Dabie–Sulu orogenic belt  
99 resulted in the complete isolation of the Paleo-Tethys Ocean from the Panthalassa Ocean.  
100 However, constraining the timing of oceanic isolation is difficult because the dating of both  
101 orogenic metamorphism and magmatism tend to postdate the onset of continental collision  
102 (Roberts and Finger, 1997; Schmädicke et al., 2018). Currently, ages of eclogites from the  
103 Dabie–Sulu orogenic belt interpreted to reflect continental collision are Triassic (250–200 Ma;  
104 Jian et al., 2012; Liu et al., 2006; Zhou et al., 2011, 2015), which would appear to indicate that  
105 the isolation of the Paleo-Tethys Ocean from the Panthalassa Ocean occurred after the Permian  
106 mass extinction (Fig. 1a). These ages, however, are inconsistent with a paleogeographic  
107 reconstruction of East Asia derived from paleontological data that argue for the amalgamation of  
108 these two major continental blocks before the end-Permian, providing a united landmass for the  
109 Cathaysian biota and facilitating the formation of a stagnant Paleo-Tethys Ocean (Algeo et al.,  
110 2011; Cao and Zheng, 2009; Metcalfe, 1998, 2006; Yin et al., 2012, 2014). Although  
111 paleomagnetic data can place constraints on such an earlier initiation of this continental collision  
112 (Fig. 1b; Huang et al., 2018), their large uncertainties (~1,000 km) might preclude pinpointing  
113 the exact timing of when the Paleo-Tethys was cut off from the Panthalassa.

114 A potentially critically important clue for solving the Paleo-Tethys oceanic isolation problem  
115 that has been missing is an understanding of the significance of the initiation of the Permo-  
116 Triassic Sulu orogenic event of East Asia. This orogenic event not only resulted in the world-  
117 famous Dabie–Sulu ultrahigh pressure metamorphism, but also greatly influenced both North  
118 and South China, causing significant crustal thickening in southern North China (Li et al., 2017c;  
119 Liu et al., 2018), and an intracontinental orogenic belt in South China (Zhao et al., 2022). Unlike  
120 the ultrahigh pressure eclogites of the Sulu orogenic belt which are insensitive to initial  
121 continental collision, rocks of this region that did not experience deep subduction might be able

122 to better constrain the time of the initial collision. This study presents new geochronological  
 123 results yielded using multiple dating techniques on low-grade metamorphic rocks in the northern  
 124 Dabie orogenic belt and high-grade rocks from within South China. In addition, we also include  
 125 a synthesis of recent studies of the Permo–Triassic metamorphism in southeastern North China,  
 126 the Cathaysia block of southeastern South China, and the Dabie–Sulu orogenic belt. The initiation  
 127 of the Permo–Triassic intracontinental orogeny as well as the timing of low-grade metamorphism  
 128 in the northern Dabie orogenic belt consistently support a new Permo–Triassic tectonic  
 129 paleogeographic reconstruction model for East Asia, with direct implications for more  
 130 definitively constraining the timing of oceanic isolation with respect to the Permian mass  
 131 extinction.



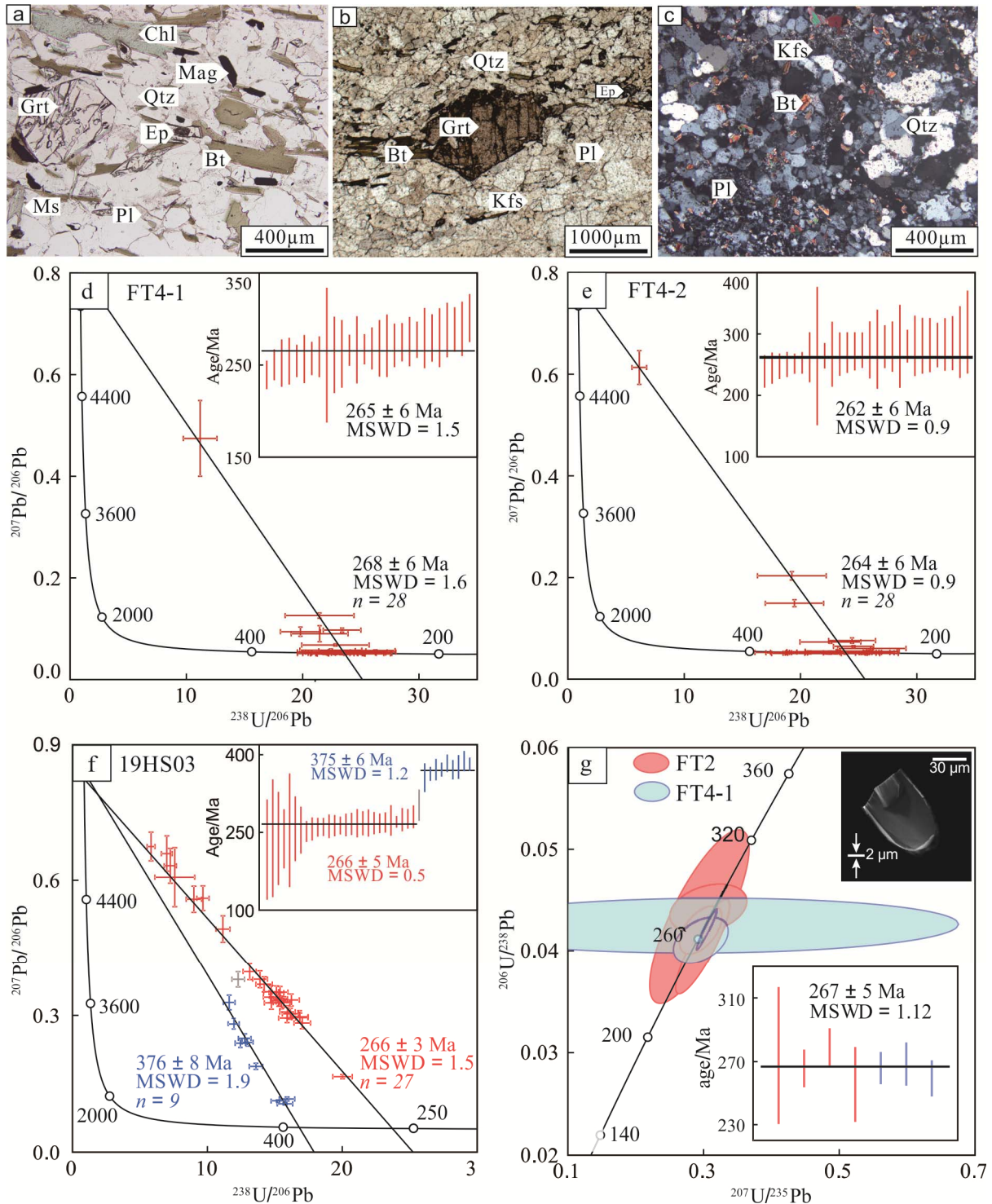
132

133 **Fig. 2.** Simplified geological map of East Eurasia. Modified after Zhao et al. (2015b, 2022).

134 **2 Geological background and samples**

135 East Asia is a composite of continental terranes including cratons/blocks of North China and  
136 South China. The North China craton (including the Korean Peninsula) is a continental block  
137 consisting of early Precambrian basement rocks tracing back to Eoarchean and experienced  
138 pervasive Neoproterozoic and Paleoproterozoic high-grade metamorphic reworkings (Wang et al.,  
139 2015; Zhai, 2011, 2014; Zhao, 2014). Its amalgamation with the South China and its subsequent  
140 decratonization are the most significant tectonic events witnessed by North China during the  
141 Phanerozoic (Wu et al., 2019; Yang et al., 2008; Zhu et al., 2012). The former tectonic event  
142 mainly affected rocks in southern and southeastern North China (along the Qinling–Dabie–Sulu  
143 orogenic belt; Fig. 2), which display Paleozoic–early Mesozoic high-pressure to ultra-high  
144 pressure metamorphism (An et al., 2018; Li et al., 2017c; Wang et al., 2014; Liu et al., 2021).  
145 Influence of the latter tectonic event is relatively more widespread, manifested by Mesozoic  
146 magmatism and thin-skinned deformation mainly in the central and eastern North China (Lin et  
147 al., 2011; Zhang et al., 2014b; Zhu et al., 2015).

148 South China was formed through the amalgamation of the Yangtze and the Cathaysia blocks  
149 during the Neoproterozoic, and is thought to have maintained its integrity ever since (Cawood et  
150 al., 2018, 2020; Li et al., 2009; Wang et al., 2013a). “Cathaysia” here has a different meaning  
151 from ‘Cathaysialand’ used in paleontological/ paleogeographic studies which refer to the much  
152 broader regions situated to the east of the Paleo-Tethys Ocean, including North China, South  
153 China, and Indochina (Metcalfe, 1998, 2006). The Yangtze block occupies the northwestern part  
154 of South China (Fig. 2), and has Archean and Paleoproterozoic basement components in its  
155 northern (Kongling) and southwestern (Cuoke near Kunming) marginal regions (Fig. 2) (Cui et  
156 al., 2021; Qiu et al., 2000; Wang et al., 2018; Ye et al., 2017; Zhang et al., 2006). Large areas of  
157 the Yangtze block remained stable during the Phanerozoic and tectonic events during the  
158 Paleozoic (South China Caledonian), and Mesozoic (Indosinian and Yanshanian) orogenic  
159 events affected mainly the marginal regions of this continental block (Faure et al., 2016; Li,  
160 1994; Li and Li, 2007; Shu et al., 2008; Wang and Liou, 1991; Xiao and He, 2005). The famous  
161 Meishan and Penglitan GSSP sections (Global Boundary Stratotype Section and Point)  
162 recording the end-Permian mass extinction occur in different parts of the Yangtze block (Fig. 2)  
163 (Cao and Zheng, 2009; Jin et al., 2000; Shen et al., 2019). The Cathaysia block is situated in the  
164 southeastern South China and is bounded by the Jiang–Shao fault with the rest of South China  
165 (Fig. 2). Early Precambrian lithologies have been discovered from different localities of this  
166 continental block (Shen et al., 2016; Xia and Xu, 2019; Zhang et al., 2021a; Zhao et al., 2015b).  
167 Metamorphism and related magmatism in the Paleozoic (also known as the South China  
168 Caledonian, 460–410 Ma), the Permo–Triassic (Indosinian), and the Late Mesozoic  
169 (Yanshanian) are each extensively developed in the Cathaysia block, and they exhibit a younging  
170 trend from northwest to southeast (Fig. 2). Both the Paleozoic and the Permo–Triassic tectonic  
171 events affected lower crustal components, as indicated by the occurrences of granulite facies  
172 rocks (Yu et al., 2003, 2005; Zhao et al., 2016, 2017, 2018), and they have both been suggested  
173 to be results of intracontinental orogens (Shu et al., 2014; Zhang et al., 2013a).



174

175 **Fig. 3.** Representative photomicrographs of the studied samples collected from the Beijiayang  
 176 zone of northern Dabie orogen (a-c) and dating results (d-g) of the studied samples from the  
 177 Beihuaiyang zone. (a) Garnet mica schist from the Foziling Group. (b) Garnet-bearing granitic  
 178 gneiss. (c) Fine-grained biotite gneiss from the Luzhengan Complex. (d-e) SIMS rutile U-Pb  
 179 dating results of the two garnet mica schist samples from the Foziling Group. (f) SIMS titanite  
 180 U-Pb dating results of the garnet-bearing granitic gneiss sample from the Luzhengan Complex.

181 (g) SIMS U-Pb dating results of the unpolished zircon grains from one garnet mica schist sample  
182 (FT4-1) of the Foziling Group and one fine-grained biotite gneiss sample of the Luzhenguan  
183 Complex. Mineral abbreviations: Grt – garnet, Ms – muscovite, Pl – plagioclase, Bt – biotite, Qtz  
184 – quartz, Chl – chlorite, Ep – epidote, Kfs – K-feldspar, Mag – magnetite.

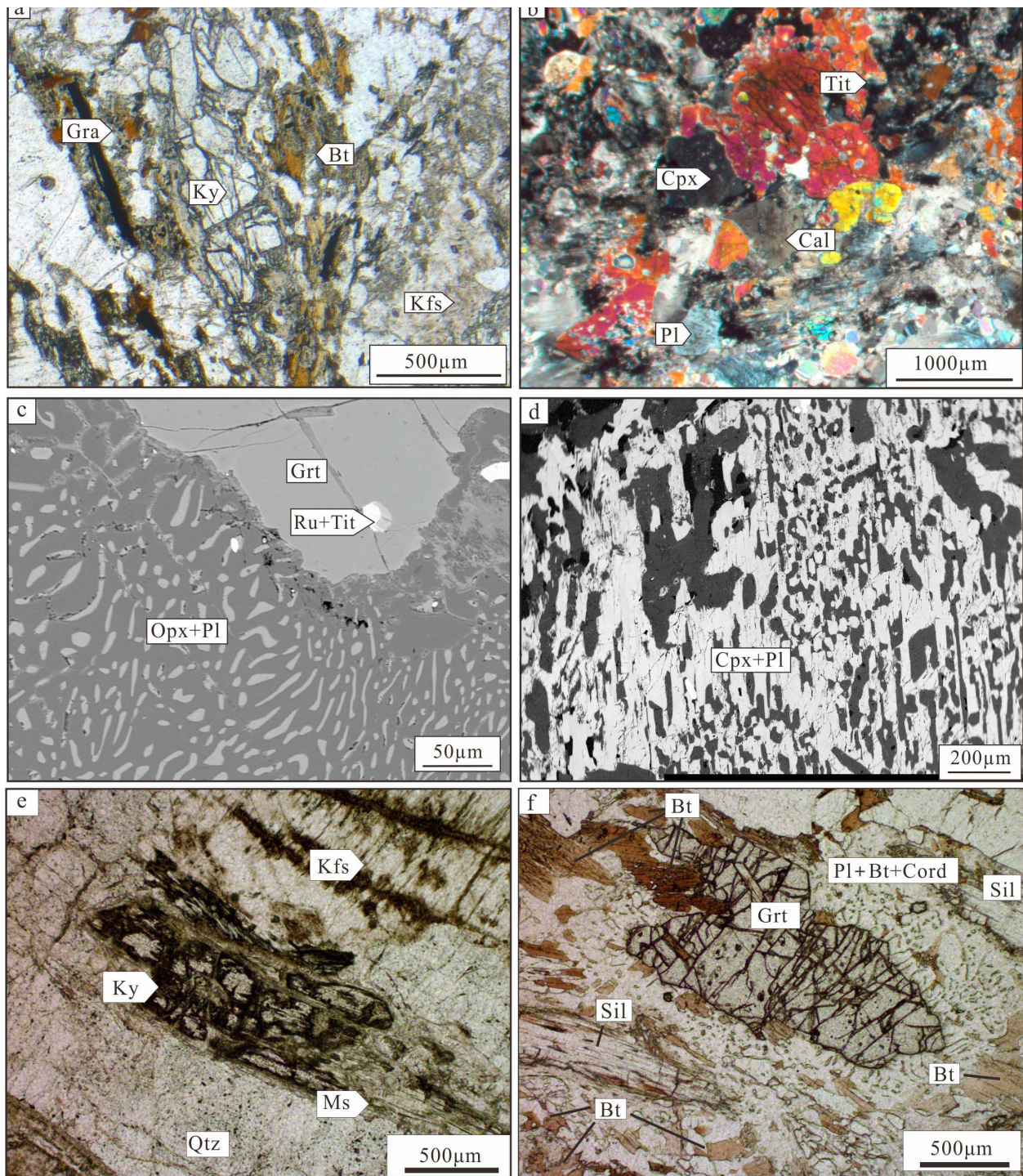
185 Southeast Asia, which is also in the Paleo-Tethys tectonic realm, consists two major  
186 continental terranes, the Indochina and the Sibumasu terranes. These two terranes have been  
187 suggested to have successively rifted off the northern margin of Gondwana during the Devonian  
188 and late Early Permian, respectively, and finally united during the Permo–Triassic (Metcalfé,  
189 2006). There were several seaways connecting the Paleo-Tethys Ocean and the Panthalassa  
190 Ocean during the Permian, with the southern connection being the branch of the Paleo-Tethys  
191 between Indochina and South China, and the northern connection being the branch between  
192 North and South China (Fig. 1a). Intense controversies exist about both the timing and  
193 mechanism of the amalgamation of South China and Indochina which disconnected the Paleo-  
194 Tethys and the Panthalassa oceans in the south (Cocks and Torsvik, 2013; Faure et al., 2016;  
195 Lepvrier et al., 2004; Metcalfé, 1998, 2006). Different studies suggested subduction polarity  
196 along the Song Ma suture of both northward and southward during the consumption of a  
197 southern branch of the Paleo-Tethys Ocean prior to the amalgamation of these two continental  
198 blocks, with proposed final collisional ages ranging widely from prior to Late Silurian (Carter  
199 and Clift, 2008), Early Carboniferous (Metcalfé, 2006, 2013), and Triassic (Cocks and Torsvik,  
200 2013; Faure et al., 2014, 2016; Zhang et al., 2014a). High-grade metamorphic rocks as well as  
201 strong deformation occurring along the Song Ma suture, and also in Vietnam, have been  
202 suggested to be products of the Indosinian orogeny in the Indochina Peninsula (Cocks and  
203 Torsvik, 2013; Faure et al., 2014, 2016; Nam et al., 2001; Roger et al., 2007; Zhang et al.,  
204 2014a). These metamorphic studies give undeniable evidence for Triassic metamorphic ages and  
205 have been widely employed to argue for Triassic collisional events between South China and  
206 Indochina (Nam et al., 2001; Roger et al., 2007; Zhang et al., 2013b). However, the geological  
207 significance of these high-grade metamorphic rocks is not unequivocal. As pointed out by Carter  
208 and Clift (2008), the Indosinian orogeny in Southeast Asia is not a Triassic mountain building  
209 event, but rather, is a tectonothermal reactivation event related to the accretion of the Sibumasu  
210 block to the Indochina block. Furthermore, palaeontological studies indicate that the distinctive  
211 Early Permian “Cathaysian” flora (*Gigantopteris*) is found in both South China and Indochina  
212 (Metcalfé, 2006), suggesting an early amalgamation of these two continental blocks prior to that  
213 time.

214 The northern seaway belonging to the Paleo-Tethys Ocean existed between North and South  
215 China during the Paleozoic, connecting the two major oceans (Fig. 1a). Geological processes  
216 within the tectonic realm of this seaway involved subduction, arc formation, back-arc extension,  
217 and the final continental collision that welded North and South China and formed the composite  
218 Paleozoic–Mesozoic Central China Orogenic belt (Liu et al., 2011; Wu and Zheng, 2013; Zhang  
219 et al., 2004; Yin and Nie, 1993). This orogenic belt is further divided into different sections and  
220 each of them exhibits different evolutionary histories (Qinling–Tongbai–Hong’an–Dabie–Sulu;  
221 Fig. 2) (Liu et al., 2011; Wu and Zheng, 2013; Zhang et al., 2004). The western section  
222 (Qinling–Tongbai–Hong’an) of the orogen shows significant Paleozoic arc–continental collisions  
223 and the final continental collisions caused mainly amphibolite facies metamorphism in the  
224 southern Qinling section during the Triassic (Fig. S1A) (Dong et al., 2011; Wu, 2009; Zhou et  
225 al., 2011, 2015). Alternatively, the eastern section (Dabie–Sulu) exhibits more obvious features

226 of continental collision between the two major continental blocks, whose ultrahigh pressure  
227 eclogites give mainly Triassic metamorphic ages and indicate Triassic continental collisional  
228 events (Fig. S1A) (Okay et al., 1989; Wang et al., 1989, 1992; Xu et al., 1992; Ye et al., 2000).  
229 Previous studies generally seem to show that the final collision of North and South China, which  
230 completely disconnected the northern seaway, occurred during the Triassic (An et al., 2018;  
231 Dong et al., 2016; Meng and Lin, 2021; Meng and Zhang, 1999; Wu and Zheng, 2013). If so,  
232 this age would apparently follow the time of the end-Permian extinction. However, the  
233 restriction of circulation of oceanic water masses does not wait until the final continental  
234 collision, and will already initiate with initial collision and the onset of crustal thickening.  
235 Besides, geochronological results from high-grade rocks tend to post-date the onset of orogenic  
236 belts, because most metamorphic zircon grains form during post-peak retrograde metamorphic  
237 stages (Roberts and Finger, 1997; Zhao et al., 2015a). On the other hand, paleontological studies  
238 found similar Late Paleozoic and Mesozoic floras and faunas in both North and South China  
239 (Metcalf, 1998, 2006; Şengör and Atayman, 2009), requiring land bridges between them and  
240 implying an early amalgamation of these continental blocks. Similar results are also indicated by  
241 paleomagnetic data (Fig. 1b) (Huang et al., 2018). Based on these considerations, it is suggested  
242 that the age of the onset of the continental collision between North and South China needs to be  
243 critically reevaluated.

244 Samples of this study were collected from the Beihuaiyang zone in the northernmost part of  
245 the Dabie orogenic belt (Fig. 2 and Fig. S1B), and the Qushan Island located on the continental  
246 shelf region of the northeast Cathaysia, South China (Fig. 2). The metamorphic rocks of the  
247 Beihuaiyang zone did not undergo deep subduction, and compared with the deeply subducted  
248 eclogite facies rocks which were then exhumed to the surface, metamorphism of these  
249 metamorphic rocks is more likely to represent the earlier phases of the continental collisional  
250 events and give more precise constraints on the initial docking of the two continental blocks. The  
251 Foziling Group and the Luzhengan Complex are the two major constituent lithological units of  
252 the Beihuaiyang zone, with both units having close affinity with the Yangtze block of South  
253 China (Chen et al., 2003; Wu et al., 2007; Zheng et al., 2005). The metamorphism they record  
254 are the direct result of the convergence between these two continental blocks. Two garnet mica  
255 schist samples (FT4-1 and -2) from the Foziling Group, one garnet-bearing granitic gneiss  
256 sample (19HS03), and one fine-grained biotite gneiss sample (FT2, Fig. S1B) from the  
257 Luzhengan Complex were dated. Sampling locations, detailed descriptions of these samples,  
258 and analytical results are included in the **Supplementary material 1**. Representative  
259 photomicrographs and dating results are presented in **Figure 3**. The mineral assemblage of Grt +  
260 Bt + Ms + Pl + Chl + Ep + Qtz in the garnet mica schist samples suggests greenschist to  
261 amphibolite facies metamorphism (Fig. 3).

262 The high-grade metamorphic rocks of the Qushan Island in South China include garnet  
263 amphibolites, garnet biotite gneiss, garnet sillimanite gneiss, and marble, all of which exhibit  
264 obvious features of anatexis and strong deformation. We identified a high-pressure granulite  
265 facies mineral assemblage of garnet + kyanite + sillimanite + K-feldspar + plagioclase + quartz  
266 from the garnet biotite gneiss occurring on Qushan Island (Fig. 4a), indicating high-grade  
267 metamorphism similar to that of the northern Wuyi terrane during the Permo–Triassic orogeny.  
268 One garnet sillimanite biotite gneiss sample (14CS01) and one leucogranitic vein sample  
269 (14CS02) were collected from this region. Detailed descriptions of the collected Qushan Island  
270 samples and other related rocks of the region are presented in the **Supplementary material 2**.



271

272 **Fig. 4.** Representative photomicrographs of high-grade metamorphic rocks from the Wuyi  
 273 terrane and Qushan Island of the South China intracontinental orogenic belt. (a) Pelitic high  
 274 pressure granulite sample collected from the Qushan Island of northern Wuyi. (b)  
 275 Metamorphosed calc-silicate sample collected from the Qushan Island. (c-d) Mafic granulite and  
 276 retrograded eclogite samples from the Wuyi terrane, showing symplectitic reactions textures  
 277 formed during decompressional retrograde metamorphic stages: Opx + Pl replacing garnet (c)  
 278 and Cpx + Pl replacing Omph (d) (modified from [Zhao et al. \(2017\)](#)). (e-f) Pelitic granulite

279 samples from the Wuyi terrane (modified from Zhao et al. (2018)). Mineral abbreviations: Opx –  
 280 orthopyroxene, Ru – rutile, Tit – titanite, Cpx – clinopyroxene, Sil – sillimanite, Ky – kyanite,  
 281 Cord – cordierite, Gra – graphite, Cal – calcite. Others are as in Fig. 3.

### 282 3 Analytical methods

283 The collected samples were crushed and separated by standard density and magnetic  
 284 techniques. Rutile, titanite, and zircon were handpicked under a microscope. Rutile samples with  
 285 rutile standards DXK ( $1782.6 \pm 2.8$  Ma, Li et al., 2013a) and JDX ( $518 \pm 4$  Ma, Li et al., 2013a),  
 286 titanite samples with standards YQ82 ( $1837.6 \pm 1.0$  Ma; Huyskens et al., 2016) and Ontario  
 287 ( $1053.5 \pm 3.1$  Ma; Spencer et al., 2013) were put together in epoxy mount, respectively. The  
 288 mounts were polished to expose the mid-sections of crystals. Zircon samples were mounted in  
 289 the epoxy with zircon standard of Plešovice ( $337.1 \pm 0.4$  Ma, Sláma et al., 2008) and Qinghu  
 290 ( $159.5 \pm 0.2$  Ma, Li et al., 2013b). In order to keep the thin overgrowth zircon rim, we did not  
 291 polish those zircon crystals but cleaned them carefully. Single-minerals U–Pb age analysis were  
 292 carried out using Secondary Ion Mass Spectrometry (CAMECA IMS 1280HR) at Institute of  
 293 Geology and Geophysics, Chinese Academy of Sciences.

294 **Rutile SIMS U–Pb dating:** The  $O_2^-$  was selected to be the primary beam, which was  
 295 accelerated at a potential of  $-13$  kV. The intensity of primary beam was about  $10\text{--}15$  nA. The  
 296 size elliptical analytical spot was  $20 \times 30$   $\mu\text{m}$ . Positive secondary ions were extracted with a  $+10$   
 297 kV potential. One electron multiplier was used to count secondary ions in peak-jumping mode.  
 298 The time of pre-sputtering was set as  $120$  s to remove the coated gold layer. The time duration  
 299 for each spot analysis is about  $15$  min. The detailed analytical procedures can be found in Li et  
 300 al. (2011). Rutile standard DXK was used to calibrate the instrument fractionation between U  
 301 and Pb, and standard JDX was used as an unknown sample to assess the quality of calibration.  
 302 Data without common lead correction was plot on Tera-Wasserburg concordia diagrams to  
 303 obtain the lower intercepted age with the concordia curve. The age of single point was after  $^{207}\text{Pb}$   
 304 correction of common lead.

305 **Titanite SIMS U–Pb dating:** The primary beam of  $O_2^-$  was accelerated at a potential of  $-13$   
 306 kV. The intensity of the primary beam was  $10\text{--}17$  nA. The analytical beam was  $20 \times 30$   $\mu\text{m}$  in  
 307 size. It took  $120$  s for pre-sputtered and  $17$  min for each spot analysis. The secondary ions were  
 308 counted by an electron multiplier in peak-jumping mode (Li et al., 2011). The counts of  $^{56}\text{Fe}^{16}\text{O}^+$   
 309 were used to calibrate the matrix effect of titanite SIMS U–Pb dating. The calibration formula is  
 310  $(^{206}\text{Pb}^+/^{238}\text{U}^+)_{\text{calibrated}} = (^{206}\text{Pb}^+/^{238}\text{U}^+)_{\text{measured}} / (^{56}\text{Fe}^{16}\text{O}^+/\text{PB})^{-0.11}$ , in which the PB is the intensity  
 311 of primary beam. The instrument fractionation between U and Pb for titanite sample is calibrated  
 312 using titanite standard YQ82, and the quality of calibration is reference to the calibration age  
 313 results of titanite standard Ontario.

314 **Unpolished zircon SIMS U–Pb dating:** The elliptical analytical spot was  $10 \times 15$   $\mu\text{m}$  in size.  
 315 Since the analyzed zircon grains were not polished, the time of pre-sputtered was increased to  
 316  $180$  s to remove the contamination of common lead. The total time duration of single point  
 317 analysis is  $\sim 15$  min. Zircon standard Plešovice was used for U/Pb instrument fractionation  
 318 calibration, and zircon standard Qinghu was used as an unknown sample to monitor the quality  
 319 of data. The common Pb calibration was performed using the value of  $^{204}\text{Pb}$ . The detailed  
 320 description of SIMS zircon U–Pb dating method is described in Li et al. (2009).

321       Uncertainties of all isotopic ratios are reported at  $1\sigma$  level, and the age are quoted with 95%  
322 confidence intervals.

323       **SHRIMP zircon U-Pb age dating:** SHRIMP zircon U-Pb age dating were carried out at  
324 Beijing SHRIMP Center, Chinese Academy of Geological Sciences, using the SHRIMP II  
325 instrument. The focused O<sub>2</sub>- beam is  $\sim 4$ nA and the standard to unknown ratio is 1:4. Five scans  
326 were used for each analysis. The analytical protocol and procedures have been detailed described  
327 by Williams (1998). Common Pb corrections were based on the measured <sup>204</sup>Pb. Uncertainties  
328 for individual analyses are quoted a  $1\sigma$ .

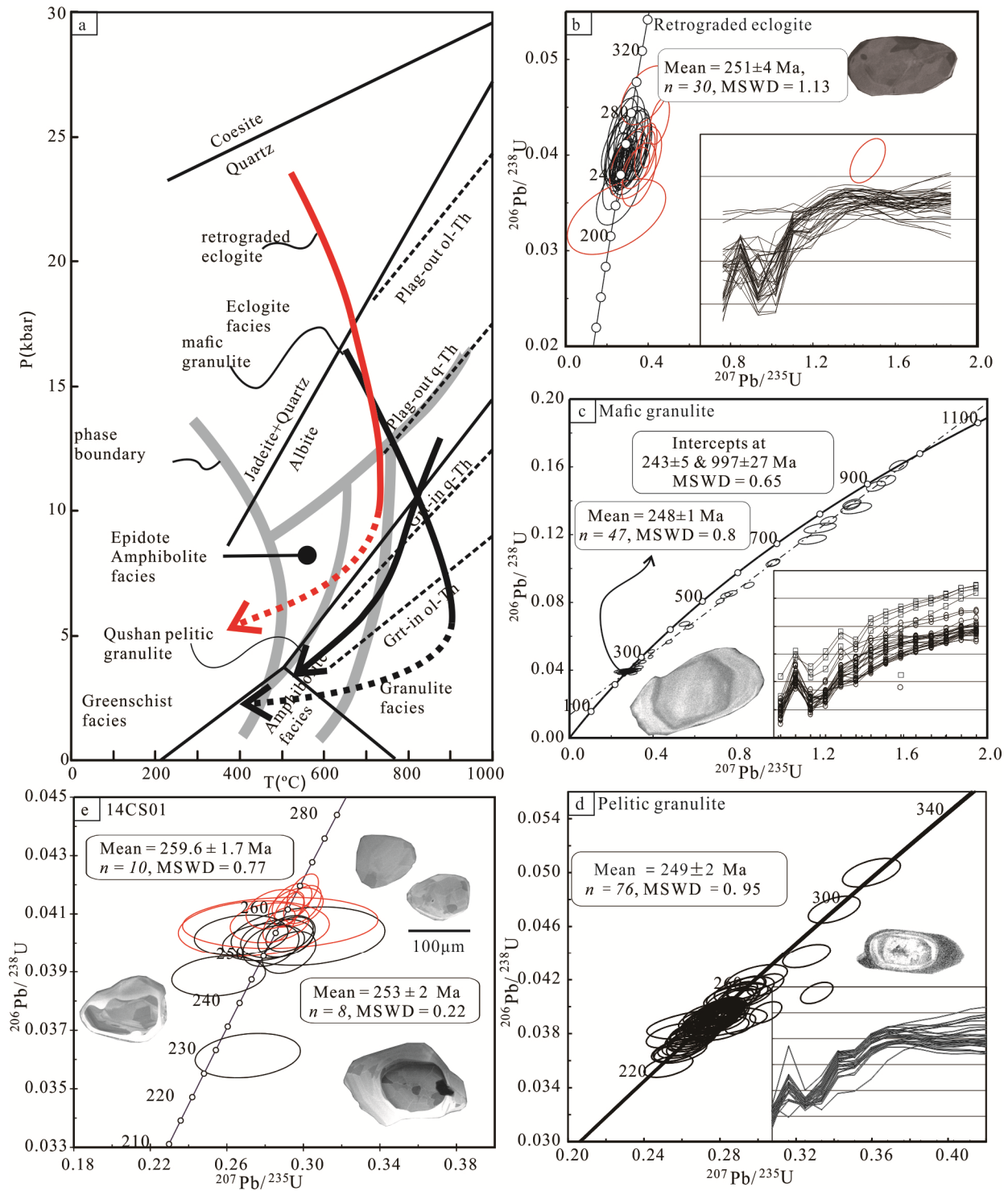
329       **Trace elements of rutile and titanite:** Analyses of mineral trace elements were performed  
330 using Agilent 7500a Inductively Coupled Plasma Mass Spectrometer coupled with 193 nm ArF-  
331 excimer laser-ablation system at Institute of Geology and Geophysics, Chinese Academy of  
332 Sciences. The analytical laser beam size was 32  $\mu$ m. The detailed analytical conditions could be  
333 referenced to Wu et al. (2018). NIST SRM 610 was used to calibrate the measured data, and  
334 USGS BCR-2G was as the data calibration quality monitoring sample. The internal standard  
335 elements for trace element content correction are Ti for rutile and Si for titanite.

## 336 4 Results

### 337 4.1 Analytical results of the northern Dabie samples

338       Detailed analytical results of the sample from the Beihuaiyang zone of the northern Dabie  
339 orogeny are presented in **Supplementary material 1** and **Fig. 3**. The rutile grains in the two garnet-  
340 mica schist samples range from 50 to 150  $\mu$ m in length. The high Nb and low Cr contents,  
341 together with low Cr/Nb ratios (0.03–0.36) (**Fig. S2** and **Table S1**) show that these rutile grains  
342 grew during metamorphism in the metapelite rocks (Meinhold, 2010). The Zr contents of rutile  
343 in FT4-1 and FT4-2 are 87–116 ppm (mean = 104 ppm) and 102–126 ppm (mean = 112 ppm),  
344 respectively, corresponding to metamorphic temperatures of 530–551 °C and 542–557 °C  
345 (Hayden et al., 2008, **Table S1**). The yielded rutile U–Pb ages for FT4-1 is  $268 \pm 6$  Ma (MSWD  
346 = 1.6) and for FT-2 is  $264 \pm 6$  Ma (MSWD = 0.94) (**Figs. 3d** and **3e**, **Table S2**).

347       Most titanite grains in granitic gneiss sample 19HS03 are homogeneous as shown in BSE  
348 images (**Fig. S3**), with Al<sub>2</sub>O<sub>3</sub> = 6.48–8.04 wt.%, Fe<sub>2</sub>O<sub>3</sub> = 0.99–1.50 wt.%, Al/Fe = 7.0–12.2, Zr =  
349 14–24 ppm. The Zr-in-titanite temperatures are estimated to be 611–635 °C (**Table S3**), but  
350 maybe overestimated because of the absence of rutile and ilmenite in rock (Hayden et al., 2007).  
351 The U–Pb age of homogeneous titanite is  $266 \pm 3$  Ma (MSWD = 1.5; **Fig. 3f**, **Table S4**), with U  
352 contents of 2–36 ppm, and Th/U ratios of 0.01–0.07. A few titanite grains display complex  
353 zoning, but show no systematic compositional variations (**Figs. S3** and **S4**). The Al<sub>2</sub>O<sub>3</sub> and Fe<sub>2</sub>O<sub>3</sub>  
354 contents for these grains are 4.96–7.88 wt.% and 0.95–2.10 wt.%, respectively, with Al/Fe =  
355 4.1–12.9. The Zr contents in titanite cores are 26–43 ppm, and the calculated Zr-in-titanite  
356 temperatures are 638–659 °C. Both types of titanite grains have high Al/Fe ratios (**Fig. S4**, **Table**  
357 **S3**), which indicate that they were formed during metamorphism (Aleinikoff et al., 2002). The  
358 U–Pb age of titanite core is  $376 \pm 8$  Ma (MSWD = 1.9; **Fig. 3f**, **Table S4**), with U = 2–36 ppm  
359 and Th/U = 0.01–0.07.



360

361 **Fig. 5.** (a) Metamorphic P-T paths of Permo-Triassic metamorphic rocks in northern Wuyi  
 362 terrane and Qushan Island. P-T paths of mafic granulite and retrograded eclogite are from Zhao  
 363 et al. (2017) and that of the Qushan Island is from Cao et al. (2022). Zircon U-Pb age dating  
 364 results of the high-grade rocks from northern Wuyi (b-d) and Qushan Island (e). Zircon age  
 365 dating results of retrograded eclogite and mafic granulite (b-c) are from Zhao et al. (2017) and  
 366 those of the pelitic granulite (d) is from Zhao et al. (2018).

367 The metamorphic overgrowth rims of zircon grains are mostly too thin for traditional  
368 analysis (Fig. 3g, S5). In this study, we directly analyzed the zircon surface without polishing  
369 them to measure the U and Pb isotopes. The unpolished zircon grains in two of the paragneiss  
370 samples (FT2 and FT4-1) are analyzed. After excluding data with high common Pb and large  
371 error of isotopic ratios, there are 54 and 45 reliable age results for samples FT2 and FT4-1,  
372 respectively (Table S5). Four unpolished zircon grains in FT2 show  $\text{Th}/\text{U} < 0.1$ , and yielded  
373 apparent  $^{206}\text{Pb}/^{238}\text{U}$  ages of  $266 \pm 6$ ,  $274 \pm 22$ ,  $279 \pm 6$ , and  $255 \pm 12$  Ma ( $1\sigma$ ), with U contents of  
374 623, 959, 425, and 1162 ppm, respectively. The weighted mean average age is  $270 \pm 8$  Ma  
375 (MSWD = 1.4; Fig. S6A). Three unpolished zircon grains in FT4-1 yielded young apparent  
376  $^{206}\text{Pb}/^{238}\text{U}$  ages of  $259 \pm 6$ ,  $266 \pm 5$ , and  $268 \pm 7$  Ma ( $1\sigma$ ), with U contents of 1759, 2252, and  
377 333 ppm, respectively. The weighted mean average age is  $264 \pm 7$  Ma (MSWD = 0.6; Fig. S6B).  
378 All the 7 young age results in the two sample gave a weighted mean average age of  $267 \pm 5$  Ma  
379 (MSWD = 1.2; Fig. 3g).

## 380 4.2 Analytical results of the South China samples

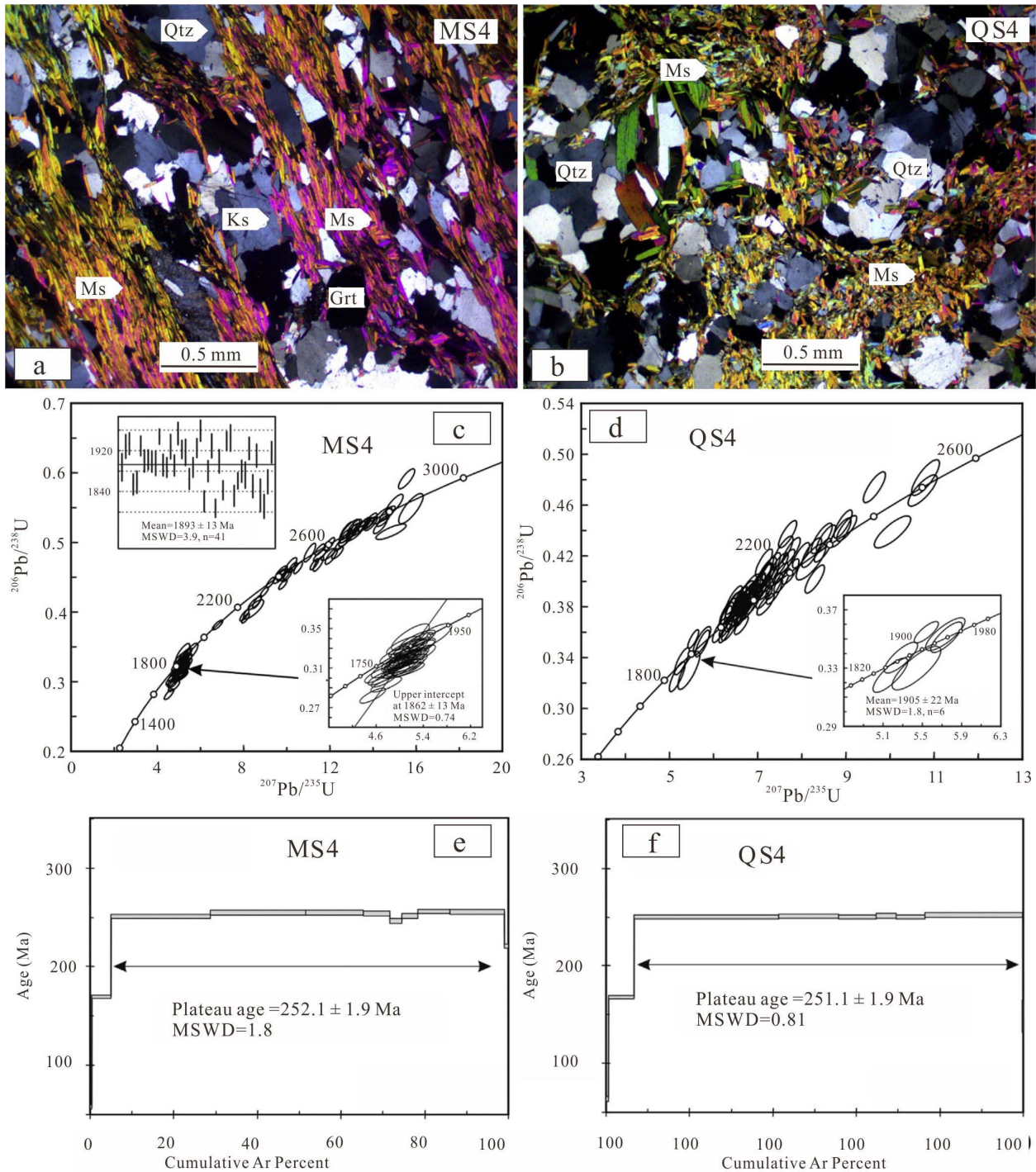
381 Analytical results (SHRIMP zircon U-Pb) of the South China samples, including the garnet  
382 sillimanite biotite (14CS01) and the leucogranitic vein (14CS02), are included in **Supplementary**  
383 **material 2**. These zircon grains exhibit typical metamorphic features, like sector zoning or  
384 without any zoning (Figs. S2.4A and B). Some of the zircon grains show core-rim structures,  
385 with both of them exhibiting typical metamorphic features (Fig. 5a). Analyzed results of these  
386 two samples are similar. Apparent ages of zircon cores from both samples are older than those of  
387 zircon rims. Apparent  $^{206}\text{Pb}/^{238}\text{U}$  ages of the 20 analyzed spots from sample 14CS02 are 246 –  
388 262 Ma while these of sample 14CS01 are mostly 246 – 264 Ma. Age results of both samples  
389 show two clusters, one at  $\sim 260$  Ma and the other at  $\sim 252$  Ma, with the former from zircon cores  
390 and the latter from other zircon domains (Figs. S2.4A and B). An older age of  $\sim 260$  Ma and a  
391 younger age of  $\sim 253$  Ma are yielded from the garnet sillimanite biotite sample, which were  
392 interpreted to represent the time of two episodes of metamorphism (Fig. 5a).

## 393 5 Discussion

### 394 5.1 Permo-Triassic metamorphism related with crustal thickening event along the East 395 Asian continent

396 Bordered to the southeast by the Sulu orogenic belt, the Jiaobei Terrane is part of the North  
397 China craton with early Precambrian crystalline basement components (Fig. 2) (Jahn et al., 2008;  
398 Liu, P. et al., 2012; Wu, M. et al., 2014; Liu F.L., et al., 2014). These components record  
399 Archean and Paleoproterozoic high-grade metamorphism during the amalgamation and  
400 cratonization of North China (Liu, P. et al., 2012; Wu, M. et al., 2014; Liu F.L., et al., 2014). The  
401 meta-sedimentary rocks of the Jingshan and Fenzishan groups occur in the southern part of the  
402 Jiaobei Terrane, in direct contact with the Sulu ultrahigh pressure orogenic belt. Part of the  
403 Jingshan and Fenzishan Group rocks were subjected to the Permo–Triassic orogenic event due to  
404 the continental collision of the North and South China (Liu et al., 2018; Cao et al., 2016). As  
405 described by Liu et al. (2018), the quartz schist and muscovite schist samples of the Jingshan  
406 Group both show Paleoproterozoic metamorphism, at 1905 Ma and 1862 Ma, respectively (Fig.  
407 6). Besides, the muscovite grains from these samples gave Late Permian  $^{40}\text{Ar}/^{39}\text{Ar}$  plateau ages  
408 of 252.1 – 251.1 Ma (Fig. 6). These Late Permian metamorphic ages represent the time of crustal

409 thickening in the southern North China Craton, due to the interactions between the North and  
 410 South China in Late Permian.



411  
 412 **Fig. 6.** Representative photomicrographs and dating results of the samples from the Jingshan  
 413 Group of the Jiaobei Terrane in the southeastern North China craton. The muscovite schist

414 (MS4) and quart schist (QS3) samples record both Paleoproterozoic and Late Permian  
415 metamorphism. These images are from [Liu et al., 2018](#).

416 The South China Permo–Triassic intracontinental orogeny affected most areas of the  
417 Cathaysia block, as indicated by pervasive deformation and magmatism ([Huang, 1960](#); [Li et al.,](#)  
418 [2006, 2017a, 2017b](#); [Li and Li, 2007](#); [Lin et al., 2018](#); [Wang et al., 2013b](#); [Xiao and He, 2005](#);  
419 [Zhang et al., 2017](#)). These geological records led [Hsü et al. \(1988\)](#) to propose that continental  
420 collisional events occurred within South China, which received extensive criticism ([Chen et al.,](#)  
421 [1991](#); [Gupta et al., 1989](#); [Rowley et al., 1989](#)). Currently, the widespread Permo-Triassic  
422 deformation and magmatism in the Cathaysia block are generally believed to have occurred in an  
423 intracontinental environment that resulted from far-field stress derived from the Central China  
424 Orogenic belt and/or the continental collision between South China and Indochina ([Li et al.,](#)  
425 [2016](#); [Song et al., 2015](#); [Wang et al., 2012, 2013b, 2021](#); [Zhang et al., 2013a](#)), and/or the  
426 subduction of the Paleo-Pacific plate ([Chu et al., 2012](#); [Li et al., 2012a, 2012b](#); [Li and Li, 2007](#);  
427 [Mao et al., 2013](#)). One particular aspect of the Permo–Triassic orogeny in South China that has  
428 been overlooked by many previous studies is the significant crustal thickening in the Wuyi  
429 segment of the northeast regions of the Cathaysia block. This segment of the intracontinental  
430 orogen is parallel with the Sulu orogenic belt ([Fig. 2](#)) and the far-field stress derived from the  
431 latter has been suggested to be a major driver of its formation ([Zhao et al., 2022](#)). Despite the  
432 strong deformation, Permo–Triassic high-grade metamorphism involving middle- to lower-crust  
433 has been rarely reported from the Cathaysia block, with most deformation involving only upper-  
434 crustal level components, as indicated by thrusting and brittle deformation ([Wang et al., 2012](#);  
435 [Zhang et al., 2013a](#)). The identification of Permo–Triassic retrograded eclogites and high-  
436 pressure granulites from the northeastern Cathaysia block imply that this Permo–Triassic  
437 orogeny is strong enough to have also affected lower crustal components ([Xia et al., 2021](#); [Zhao](#)  
438 [et al., 2017, 2018](#)). Both these mafic rocks and the metasedimentary rocks preserve high-pressure  
439 granulite facies mineral assemblages of garnet + clinopyroxene + orthopyroxene + plagioclase +  
440 quartz, and garnet + kyanite + sillimanite + biotite + K-feldspar + plagioclase + quartz,  
441 respectively ([Fig. 4](#)). Decompressional reaction textures around garnet grains in the mafic and  
442 pelitic granulites ([Fig. 4](#); the intergrowths of fine-grained clinopyroxene + plagioclase, and  
443 orthopyroxene + plagioclase in mafic granulites and intergrowth of plagioclase + cordierite +  
444 biotite in pelitic granulites) indicate significant uplift during later retrograde metamorphic stages.  
445 Eclogite facies metamorphic conditions and clockwise  $P$ – $T$  paths were extracted from these  
446 rocks, with metamorphic peak pressures of ~23–24 Kbar ([Fig. 5e](#)) ([Zhao et al., 2017](#)). Zircon U-  
447 Pb dating of these high-grade rocks indicates Triassic metamorphic ages of 251–248 Ma ([Figs.](#)  
448 [5b, c and d, Zhao et al., 2017](#)).

449 The South China Permo–Triassic high-grade metamorphism is not just confined to the  
450 northern Wuyi terrane ([Fig. 2, Zhao et al., 2022](#)), but also occur in the Yunkai terrane situated in  
451 the southwest Cathaysia block, with Triassic metamorphic ages varying between 251 Ma and  
452 230 Ma ([Fig. 2](#)) ([Zhao et al., 2015b](#)). The Permo–Triassic high-grade metamorphic rocks  
453 identified from the Qushan Island represent the northeast extension of the Permo-Triassic  
454 orogenic event in northeast South China ([Fig. 2](#)). SIMS zircon U-Pb age dating results of the  
455 high-grade metamorphic rocks of the Qushan Island show Permian metamorphic ages of ca. 260  
456 Ma ([Fig. 5a](#)), consistent with previously published data ([Cao et al., 2022](#); [Jiang et al., 2016](#)).  
457 Thus, Permo–Triassic metamorphism of eastmost Cathaysia occurred earlier than the formation  
458 of the high-grade rocks in the inland regions mentioned above and firmly indicates a Permian

459 onset of the South China Permo–Triassic intracontinental orogeny. For the metamorphic rocks of  
460 the Beihuaiyang zone in northern Dabie orogenic belt, SIMS rutile U-Pb dating of the two garnet  
461 mica schist samples give consistent Permian metamorphic ages of ca. 265 Ma (Figs. 3d and e).  
462 SIMS titanite U-Pb dating of the garnet-bearing granitic gneiss sample gives a Permian  
463 metamorphic age of 266 Ma (Fig. 3f). SIMS zircon U-Pb dating on the unpolished thin (~2µm)  
464 metamorphic zircon rims of the garnet mica schist and the fine-grained biotite gneiss samples  
465 shows uniform Permian metamorphic ages of ca. 267 Ma (Fig. 3g). Considering that such low-  
466 grade metamorphism is the result of crustal thickening due to continental collision, these  
467 metamorphic ages thus appear to indicate a Middle Permian initiation of the Dabie–Sulu  
468 orogenic belt, or even earlier. To sum up, Permian metamorphic ages, which are all closely  
469 related with crustal thickening because of the continental collision between the South and North  
470 China, have been identified from the southern North China, the northern Dabie orogen and the  
471 South China. These Permian metamorphic ages collectively indicate Permian crustal thickening  
472 events along East Asian continent.

## 473 **5.2 Permian initiation of the continental collision and restrictions on oceanic circulations**

474 There is currently a paradox between the paleogeographic reconstructions of South China and  
475 neighboring continents as based on evidence from paleontological and geological studies.  
476 Paleontological affinities argue that North and South China amalgamated before the Permian  
477 mass extinction, depicting a united landmass for the “Cathaysian” biota as well as isolating the  
478 Paleo-Tethys from the Panthalassa Ocean with this united land bridge (Algeo et al., 2010; Algeo  
479 and Twitchett, 2010; Metcalfe, 1998, 2006; Şengör and Atayman, 2009). On the other hand,  
480 previous studies of regional tectonics suggest that the final amalgamation occurred during the  
481 Triassic, postdating the end-Permian extinction (An et al., 2018; Dong et al., 2016; Meng and  
482 Lin, 2021; Meng and Zhang, 1999; Wu and Zheng, 2013).

483 The continental collision between North and South China is the most significant tectonic event  
484 that occurred in East Asia during the Paleozoic–Mesozoic (Yin and Nie, 1993; Liu et al., 2011;  
485 Wu and Zheng, 2013; Zhang et al., 1996, 2004; Meng and Zhang, 1999). This event not only  
486 resulted in the ultrahigh pressure metamorphism in the Central China Orogenic belt, but also  
487 caused crustal thickening events in both North and South China, like the Permo–Triassic  
488 intracontinental orogeny in South China (Zhao et al., 2022). Crustal thickening of the southern  
489 North China is implied by the Late Permian metamorphic overprinting shown by the early  
490 Precambrian basement components of the Jiaobei Terrane, and the initiation of crustal thickening  
491 should predate their Late Permian Ar-Ar age of ca. 252 Ma (Fig. 6, Liu et al., 2018). The  
492 Beihuaiyang zone in northern Dabie orogen was not subjected to deep subduction and the  
493 geochronological dating of samples from the Beihuaiyang zone gives coherent metamorphic ages  
494 of ca. 267 Ma (Fig. 3). The metamorphism recorded by these lithological units indicates that they  
495 were transported to mid-crustal level during continental collision. Their metamorphic ages  
496 indicate crustal thickening during the Permian, prior to crustal thickening in southeastern North  
497 China.

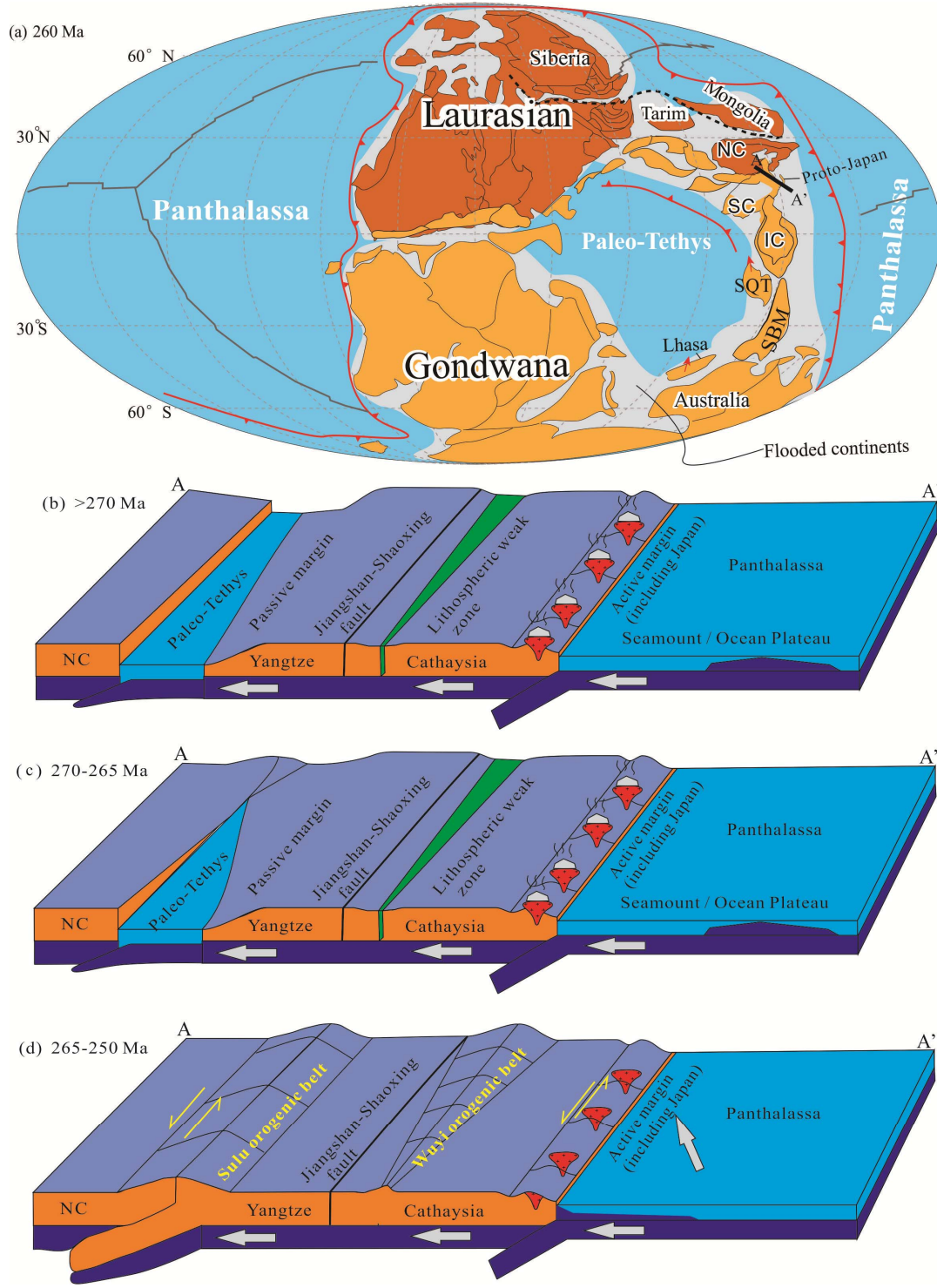
498 Permo–Triassic high-grade metamorphism within the Wuyi segment of the South China  
499 intracontinental orogen substantiates the Permian continental collision between North and South  
500 China from another perspective. The northeast–southwest striking Wuyi segment of the  
501 intracontinental orogenic belt is sandwiched by the Dabie–Sulu orogenic belt to the north (and

502 northwest) and by the the Paleo-Pacific subduction zone to the southeast (Fig. 2). Both these  
503 plate-boundary interactions contributed to the formation of this intracontinental orogeny, but the  
504 Dabie–Sulu orogenic belt was the major driver (Zhao et al., 2022; Chu et al., 2012; Li et al.,  
505 2012a, 2012b; Li and Li, 2007; Mao et al., 2013). The high-grade metamorphism on Qushan  
506 Island of the northern Wuyi orogenic belt at ca. 260 Ma apparently predates the Triassic UHP  
507 eclogite facies metamorphism along the Dabie–Sulu orogenic belt, but postdates the Permian  
508 metamorphism of northern Dabie orogenic belt as shown by the metamorphic rocks within the  
509 Beihuaiyang zone. From northeast to southwest, high-grade metamorphism of the Wuyi  
510 intracontinental orogen shows a younging trend (Fig. 2). Such a younging trend suggests that the  
511 onset of the intracontinental orogeny started from the northeast of South China and propagated to  
512 the southwest. This inferred geometry of the intracontinental orogenic belt is consistent with the  
513 generally accepted model of the Central China Orogenic belt, where the amalgamation of North  
514 and South China initiated in the east and gradually propagated to the west (Fig. 1b) (Gilder et al.,  
515 1999; Huang et al., 2018; Oh, 2015; Yin and Nie, 1993).

516 Based on our synthesis and new data, we propose a new tectonic model for the amalgamation  
517 of North and South China during the Permo–Triassic (Fig. 7). The prior South China Paleozoic  
518 Orogeny (ca. 460–410 Ma) stabilized most of South China after the Neoproterozoic Nanhua rift  
519 (Li et al., 2017a; Wang et al., 2013b), which left behind a lithospheric weak zone (Fig. 7b) (Zhao  
520 et al., 2022). Initial continental collision between North and South China occurred along the  
521 Dabie–Sulu orogenic belt (eastern segment of the Central China Orogenic belt), resulting in the  
522 crustal thickening in the Beihuaiyang zone and also in southeastern North China (the low-grade  
523 metamorphism of Beihuaiyang zone at ca. 267 Ma; Fig. 7c). Far-field stress derived from the  
524 Dabie–Sulu orogenic belt in the north, as well as the convergence of the paleo-Pacific plate in  
525 the southeast facilitated the formation of the Wuyi intracontinental orogenic belt along the pre-  
526 existing lithospheric weak zone (Fig. 7d) (Li et al., 2006; Zhao et al., 2022). Metamorphic ages  
527 of the high-grade rocks in different regions of this orogenic belt show that the onset of this  
528 orogeny started in the northeast and then propagated westward (Huang et al., 2018; Yin and Nie,  
529 1993). Continued continental collision between North and South China along the Dabie–Sulu  
530 orogenic belt caused significant tectonic stress, which not only resulted in the deep subduction of  
531 the Yangtze continental crust underneath the southern margin of North China, but also stabilized  
532 the lithospheric weak zone within South China, forming the Permo–Triassic intracontinental  
533 orogenic belt (Fig. 7). Significant crustal thickening occurred in the Wuyi terrane of Cathaysia,  
534 parallel with the Sulu orogenic belt (Fig. 2).

535 The Permo–Triassic orogenic belts in southeastern North China, within South China, and along  
536 the Dabie-Sulu orogen thus effectively isolated the Paleo-Tethys Ocean from the Panthalassa  
537 Ocean along the whole eastern front of Eurasia. Ocean circulation became severely restricted  
538 between these once contiguous oceans (Fig. 7a). Based on this refined timing of orogenic events,  
539 restricted ocean circulation between the Paleo-Tethys Ocean and the Panthalassa therefore  
540 occurred in Permian time and thus likely played a preconditioning role for the severity of the  
541 Permian mass extinction in the critical region. This restriction might also suggest a role for the  
542 Panthalassa Ocean in providing refugia for Triassic survivors and biospheric recovery. This new  
543 tectonic model of the Paleo-Tethys realm and its role in leadup to the end-Permian extinction in  
544 the region is in good accordance with the distinct features of the two Permian oceans as well as  
545 their paleontological records. From a continental perspective, the collision of North and South  
546 China also represents the final uniting of major continental blocks during the time of

547 supercontinent Pangea and the formation of the subduction girdle around the supercontinent (Fig.  
 548 7a) (Li et al., 2019). With a deadly combination of both restricted global ocean circulation and a  
 549 huge amount of volcanic emissions from the ring of fire (subduction girdle), the occurrence of a  
 550 global biospheric crisis at this time is perhaps not surprising.



552 **Fig. 7.** (a) Late Permian reconstruction of Laurasia. Note the proximity of North and South  
 553 China shown here, unlike in the reconstruction of Figure 1a, is advocated in this study to have  
 554 been already established by ca. 260 Ma, i.e., in the leadup to the Permian mass extinction.  
 555 Modified after Wu et al. (2020). (b-d) Tectonic model showing the amalgamation of the North  
 556 and South China blocks, and the formation of the South China Permo-Triassic intracontinental  
 557 orogen in the Wuyi terrane. NCC – North China craton.

## 558 **6 Conclusions**

559 Permo–Triassic metamorphism due to crustal thickening in southeastern North China, the  
 560 intracontinental orogeny of South China, and low-grade metamorphism in the northern Dabie  
 561 orogenic belt were all results of the amalgamation of North and South China in East Asia.  
 562 Therefore, while the timing of the low-grade metamorphism in the northern Dabie orogenic belt  
 563 provides direct evidence for the amalgamation process, the initiation of the intracontinental  
 564 orogeny in South China and crustal thickening in southeastern North China can independently  
 565 substantiate the initial timing of Permian amalgamation from other perspectives. Metamorphic  
 566 ages of lithologies from these different localities provide coherent clues for Middle Permian  
 567 continental collision (ca. 270 Ma), rather than during Triassic as previously suggested based on  
 568 exhumed ultrahigh pressure eclogite facies rocks. Thus, continental collisions and the formation  
 569 of orogenic belts in East Asia isolated the Paleo-Tethys Ocean from the Panthalassa Ocean  
 570 before the end-Permian mass extinction. After this isolation, the poorly mixed Paleo-Tethys  
 571 Ocean gradually became a dead sea, thereby preconditioning and facilitating the end-Permian  
 572 biospheric crisis in the region.

## 573 **Acknowledgments**

574 The authors declare no conflicts of interest.

575 The manuscript benefitted from discussions with Profs. Xianhua Li, Xiaoxiao Ling, Guoqiang

576 Tiang, and Yu Liu helped with analysis. This work was funded by the National Natural Science

577 Foundation of China (grant nos. 41872197 and 41890834).

578

## 579 **References**

- 580 Aleinikoff, J. N., Wintsch, R. P., Fanning, C. M. & Dorais, M. J. 2002. U-Pb geochronology of zircon and  
 581 polygenetic titanite from the Glastonbury Complex, Connecticut, USA: an integrated SEM, EMPA, TIMS, and  
 582 SHRIMP study. *Chemical Geology* **188**, 125-147.
- 583 Algeo, T., Shen, Y., Zhang, T., Lyons, T., Bates, S., Rowe, H. & Nguyen, T. K. T. 2008. Association of <sup>34</sup>S-depleted  
 584 pyrite layers with negative carbonate  $\delta^{13}\text{C}$  excursions at the Permian-Triassic boundary: Evidence for upwelling  
 585 of sulfidic deep-ocean water masses. *Geochemistry, Geophysics, Geosystems* **9**, doi:10.1029/2007GC001823.
- 586 Algeo, T. J., Hinnov, L., Moser, J., Maynard, J. B., Elswick, E., Kuwahara, K. & Sano, H. 2010. Changes in  
 587 productivity and redox conditions in the Panthalassic Ocean during the latest Permian. *Geology* **38**, 187-190.
- 588 Algeo, T. J., Kuwahara, K., Sano, H., Bates, S., Lyons, T., Elswick, E., Hinnov, L., Ellwood, B., Moser, J. &  
 589 Maynard, J. B. 2011. Spatial variation in sediment fluxes, redox conditions, and productivity in the Permian–  
 590 Triassic Panthalassic Ocean. *Palaeogeography, Palaeoclimatology, Palaeoecology* **308**, 65-83.
- 591 Algeo, T. J. & Twitchett, R. J. 2010. Anomalous Early Triassic sediment fluxes due to elevated weathering rates and

- 592 their biological consequences. *Geology* **38**, 1023-1026.
- 593 An, S.-C., Li, S.-G. & Liu, Z. 2018. Modification of the Sm-Nd isotopic system in garnet induced by retrogressive  
594 fluids. *Journal of Metamorphic Geology*, DOI: 10.1111/jmg.12426.
- 595 Burgess, S. D. & Bowring, S. A. 2015. High-precision geochronology confirms voluminous magmatism before,  
596 during, and after Earth's most severe extinction. *Science Advances* **1**, e1500470.
- 597 Cao, C., Love, G. D., Hays, L. E., Wang, W., Shen, S. & Summons, R. E. 2009. Biogeochemical evidence for  
598 euxinic oceans and ecological disturbance presaging the end-Permian mass extinction event. *Earth and Planetary  
599 Science Letters* **281**, 188-201.
- 600 Cao, C. & Zheng, Q. 2009. Geological event sequences of the Permian-Triassic transition recorded in the  
601 microfacies in Meishan section. *Science in China Series D: Earth Sciences* **52**, 1529-1536.
- 602 Cao, H., Vervoort, J., Wang, D., Li, G. & Neill, O. 2016. Triassic monazite ages and its geological significance of  
603 garnet-mica schist in Fenzishan Group, Jiaobei Massif. *Acta Petrologica Sinica* **32**, 3800-3816 In Chinese with  
604 English abstract.
- 605 Cao, Y., Zhou, X. & Liu, J. 2022. Discovery of high pressure granulite in the Daqu Island, East China Sea and its  
606 tectonic implications. *Journal of Jilin University Earth Science Edition*, doi: 10.13278/j.cnki.jjuese.20210343 In  
607 Chinese with English abstract.
- 608 Carter, A. & Clift, P. D. 2008. Was the Indosinian orogeny a Triassic mountain building or a thermotectonic  
609 reactivation event? *Comptes Rendus Geoscience* **340**, 83-93.
- 610 Carter, A., Roques, D., Bristow, C. & Kinny, P. 2001. Understanding Mesozoic accretion in Southeast Asia:  
611 significance of Triassic thermotectonism Indosinian orogeny in Vietnam. *Geology* **29**, 211.
- 612 Cawood, P. A., Wang, W., Zhao, T., Xu, Y., Mulder, J. A., Pisarevsky, S. A., Zhang, L., Gan, C., He, H., Liu, H., Qi,  
613 L., Wang, Y., Yao, J., Zhao, G., Zhou, M.-F. & Zi, J.-W. 2020. Deconstructing South China and consequences for  
614 reconstructing Nuna and Rodinia. *Earth-Science Reviews* **204**.
- 615 Cawood, P. A., Zhao, G., Yao, J., Wang, W., Xu, Y. & Wang, Y. 2018. Reconstructing South China in Phanerozoic  
616 and Precambrian supercontinents. *Earth-Science Reviews* **186**, 173-194.
- 617 Chapman, T., Milan, L. A., Metcalfe, I., Blevin, P. L. & Crowley, J. 2022. Pulses in silicic arc magmatism initiate  
618 end-Permian climate instability and extinction. *Nature Geoscience* **15**, 411-416.
- 619 Chen, F., Guo, J. H., Jiang, L. L., Siebel, W., Cong, B. & Satir, M. 2003. Provenance of the Beihuaiyang lower-grade  
620 metamorphic zone of the Dabie ultrahigh-pressure collisional orogen, China: evidence from zircon ages. *Journal  
621 of Asian Earth Sciences* **22**, 343-352.
- 622 Chu, Y., Faure, M., Lin, W., Wang, Q. & Ji, W. 2012. Tectonics of the Middle Triassic intracontinental Xuefengshan  
623 Belt, South China: new insights from structural and chronological constraints on the basal décollement zone.  
624 *International Journal of Earth Sciences* **101**, 2125-2150.
- 625 Clarkson, M. O., Kasemann, S. A., Wood, R. A., Lenton, T. M., Daines, S. J., Richoz, S., Ohnemüller, F., Meixner,  
626 A., Poulton, S. W. & Tipper, E. T. 2015. Ocean acidification and the Permo-Triassic mass extinction. *Science* **348**,  
627 229-232.
- 628 Cocks, L. R. M. & Torsvik, T. H. 2013. The dynamic evolution of the Palaeozoic geography of eastern Asia. *Earth-  
629 Science Reviews* **117**, 40-79.
- 630 Cui, X., Wang, J., Wang, X.-C., Wilde, S. A., Ren, G., Li, S., Deng, Q., Ren, F. & Liu, J. 2021. Early crustal  
631 evolution of the Yangtze Block: Constraints from zircon U-Pb-Hf isotope systematics of 3.1–1.9 Ga granitoids in  
632 the Cuoque Complex, SW China. *Precambrian Research* **357**.
- 633 Davydov, V. I. & Karasev, E. V. 2021. The Influence of the Permian-Triassic Magmatism in the Tunguska Basin,  
634 Siberia on the Regional Floristic Biota of the Permian-Triassic Transition in the Region. *Frontiers in Earth  
635 Science* **9**.
- 636 Dong, Y., Yang, Z., Liu, X., Sun, S., Li, W., Cheng, B., Zhang, F., Zhang, X., He, D. & Zhang, G. 2016. Mesozoic  
637 intracontinental orogeny in the Qinling Mountains, central China. *Gondwana Research* **30**, 144-158.
- 638 Dong, Y., Zhang, G., Neubauer, F., Liu, X., Genser, J. & Hauzenberger, C. 2011. Tectonic evolution of the Qinling  
639 orogen, China: Review and synthesis. *Journal of Asian Earth Sciences* **41**, 213-237.
- 640 Erwin, D. H. 1990. The end permian mass extinction. *Annu. Rev. Ecol. Syst* **21**, 69-91.
- 641 Erwin, D. H., Bowring, S. A. & Yügan, J. 2002. End-Permian mass extinction: a review. In: Koeberl, C. &  
642 MacLeod, K. G. eds. *Catastrophic events and mass extinction: impacts and beyond*. Boulder, Colorado:  
643 Geological Society of America Special Paper, 363-383.
- 644 Fan, J.-X., Shen, S.-Z., Erwin, D. H., Sadler, P. M., MacLeod, N., Cheng, Q.-M., Hou, X.-D., Yang, J., Wang, X.-d.,  
645 Wang, Y., Zhang, H., Chen, X., Li, G.-x., Shi, Y.-c., Yuan, D.-x., Chen, Q., Zhang, L.-n., Li, C. & Zhao, Y.-y.  
646 2020. A high-resolution summary of Cambrian to Early Triassic marine invertebrate biodiversity. *Science* **367**,  
647 272-277.

- 648 Faure, M., Lepvrier, C., Nguyen, V. V., Vu, T. V., Lin, W. & Chen, Z. 2014. The South China block-Indochina  
649 collision: Where, when, and how? *Journal of Asian Earth Sciences* **79**, 260-274.
- 650 Faure, M., Lin, W., Chu, Y. & Lepvrier, C. 2016. Triassic tectonics of the Ailaoshan Belt SW China: Early Triassic  
651 collision between the South China and Indochina Blocks, and Middle Triassic intracontinental shearing.  
652 *Tectonophysics* **683**, 27-42.
- 653 Gilder, S. A., Leloup, P. H., Courtillot, V., Chen, Y., Coe, R. S., Zhao, X., Xiao, W., Halim, N., Cogné, J.-P. & Zhu,  
654 R. 1999. Tectonic evolution of the Tancheng-Lujiang Tan-Lu fault via Middle Triassic to Early Cenozoic  
655 paleomagnetic data. *Journal of Geophysical Research: Solid Earth* **104**, 15365-15390.
- 656 Gupta, S., Rodgers, J., Hsü, K. J., Shu, S., Jiliang, L., Haihong, C., Haipo, P. & Sengor, A. 1989. Comments and  
657 Reply on " Mesozoic overthrust tectonics in south China". *Geology* **17**, 669-673.
- 658 Hsü, K. J., Sun, S., Li, J., Chen, H., Pen, H. & Sengor, A. 1988. Mesozoic overthrust tectonics in south China.  
659 *Geology* **16**, 418-421.
- 660 Huang, B., Yan, Y., Piper, J. D. A., Zhang, D., Yi, Z., Yu, S. & Zhou, T. 2018. Paleomagnetic constraints on the  
661 paleogeography of the East Asian blocks during Late Paleozoic and Early Mesozoic times. *Earth-Science Reviews*  
662 **186**, 8-36.
- 663 Huang, J. 1960. Preliminary summarization of geologic tectonics in China. *Acta Geologica Sinica in Chinese* **40**, 1-  
664 37.
- 665 Huyskens, M.H., Yin, Q.Z., Li, Q.L., Li, X.H., Liu, Y., Tang, G.Q., 2016, In Search of New Monazite and Titanite  
666 Standard Minerals for In Situ U-Pb Geochronology. 47<sup>th</sup> *Lunar and Planetary Science Conference*.
- 667 Isozaki, Y. 1997. Permo-Triassic Boundary Superanoxia and Stratified Superocean: records from lost deep sea.  
668 *Science* **276**, 235-238.
- 669 Jahn, B. m., Liu, D., Wan, Y., Song, B. & Wu, J. 2008. Archean crustal evolution of the Jiaodong Peninsula, China,  
670 as revealed by zircon SHRIMP geochronology, elemental and Nd-isotope geochemistry. *American Journal of*  
671 *Science* **308**, 232-269.
- 672 Jian, P., Kröner, A. & Zhou, G. 2012. SHRIMP zircon U–Pb ages and REE partition for high-grade metamorphic  
673 rocks in the North Dabie complex: Insight into crustal evolution with respect to Triassic UHP metamorphism in  
674 east-central China. *Chemical Geology* **328**, 49-69.
- 675 Jiang, Y., Xing, G., Yuan, Q., Zhao, X., Duan, Z. & Dong, X. 2016. The first discovery of Permian metamorphic  
676 rocks in Zhoushan Islands, Zhejiang Province. *Geological Bulletin of China* **35**, 1046-1055 In Chinese with  
677 English abstract.
- 678 Jin, Y. G., Wang, Y., Wang, W., Shang, Q. H., Cao, C. Q. & Erwin, D. H. 2000. Pattern of Marine Mass Extinction  
679 Near the Permian-Triassic boundary in South China. *Science* **289**, 432-436.
- 680 Lepvrier, C., Maluski, H., Van Tich, V., Leyreloup, A., Truong Thi, P. & Van Vuong, N. 2004. The Early Triassic  
681 Indosinian orogeny in Vietnam Truong Son Belt and Kontum Massif; implications for the geodynamic evolution  
682 of Indochina. *Tectonophysics* **393**, 87-118.
- 683 Li, J., Dong, S., Zhang, Y., Zhao, G., Johnston, S. T., Cui, J. & Xin, Y. 2016. New insights into Phanerozoic tectonics  
684 of south China: Part 1, polyphase deformation in the Jiuling and Lianyunshan domains of the central Jiangnan  
685 Orogen. *Journal of Geophysical Research: Solid Earth* **121**, 3048-3080.
- 686 Li, J., Zhang, Y., Zhao, G., Johnston, S. T., Dong, S., Koppers, A., Miggins, D. P., Sun, H., Wang, W. & Xin, Y.  
687 2017a. New insights into Phanerozoic tectonics of South China: Early Paleozoic sinistral and Triassic dextral  
688 transpression in the east Wuyishan and Chencai domains, NE Cathaysia. *Tectonics* **36**, 819-853.
- 689 Li, J., Zhao, G., Johnston, S. T., Dong, S., Zhang, Y., Xin, Y., Wang, W., Sun, H. & Yu, Y. 2017b. Permo-Triassic  
690 structural evolution of the Shiwandashan and Youjiang structural belts, South China. *Journal of Structural*  
691 *Geology* **100**, 24-44.
- 692 Li, S., Jahn, B.-m., Zhao, S., Dai, L., Li, X., Suo, Y., Guo, L., Wang, Y., Liu, X., Lan, H., Zhou, Z., Zheng, Q. &  
693 Wang, P. 2017c. Triassic southeastward subduction of North China Block to South China Block: Insights from  
694 new geological, geophysical and geochemical data. *Earth-Science Reviews* **166**, 270-285.
- 695 Li, X., Liu, Y., Li, Q., Guo, C., and Chamberlain, K. R., 2009, Precise determination of Phanerozoic zircon Pb/Pb  
696 age by multicollector SIMS without external standardization. *Geochemistry Geophysics Geosystems* **10**, 4, n/a-  
697 n/a.
- 698 Li, Q., Wu, F., Li, X., Qiu, Z., Liu, Y., Yang, Y., and Tang, G., 2011, Precisely dating Paleozoic kimberlites in the  
699 North China Craton and Hf isotopic constraints on the evolution of the subcontinental lithospheric mantle.  
700 *Lithos* **126**, 127-134.
- 701 Li Q., Yang Y., Shi Y., Lin W., 2013a. Eclogite rutile U-Pb dating: constraint for formation and evolution of  
702 continental collisional orogen. *Chinese Science Bulletin* **58**, 2279–2284, doi: 10.1360/972013-590.

- 703 Li, X., Tang, G., Gong, B., Yang, Y., Hou, K. J., Hu, Z., Li, Q., Liu, Y., and Li, W., 2013b. Qinghu zircon: A  
 704 working reference for microbeam analysis of U-Pb age and Hf and O isotopes. *Chinese Science Bulletin* 58,  
 705 4647-4654.
- 706 Li, X. H., Li, W. X., Li, Z. X., Lo, C. H., Wang, J., Ye, M. F. & Yang, Y. H. 2009. Amalgamation between the  
 707 Yangtze and Cathaysia Blocks in South China: Constraints from SHRIMP U–Pb zircon ages, geochemistry and  
 708 Nd–Hf isotopes of the Shuangxiwu volcanic rocks. *Precambrian Research* 174, 117-128.
- 709 Li, X. H., Li, Z. X., Li, W. X. & Wang, Y. 2006. Initiation of the Indosinian orogeny in South China: Evidence for a  
 710 Permian magmatic arc on Hainan Island. *The Journal of Geology* 114, 341-353.
- 711 Li, Z.-X. 1994. Collision between the North and South China blocks: a crustal-detachment model for suturing in the  
 712 region east of the Tanlu fault. *Geology* 22, 739-742.
- 713 Li, X.-H., Li, Z.-X., He, B., Li, W.-X., Li, Q.-L., Gao, Y. & Wang, X.-C. 2012a. The Early Permian active  
 714 continental margin and crustal growth of the Cathaysia Block: In situ U–Pb, Lu–Hf and O isotope analyses of  
 715 detrital zircons. *Chemical Geology* 328, 195-207.
- 716 Li, Z.-X., Li, X.-H., Chung, S.-L., Lo, C.-H., Xu, X. & Li, W.-X. 2012b. Magmatic switch-on and switch-off along  
 717 the South China continental margin since the Permian: Transition from an Andean-type to a Western Pacific-type  
 718 plate boundary. *Tectonophysics* 532-535, 271-290.
- 719 Li, Z. X. & Li, X. H. 2007. Formation of the 1300-km-wide intracontinental orogen and postorogenic magmatic  
 720 province in Mesozoic South China: A flat-slab subduction model. *Geology* 35, 179-182.
- 721 Li, Z. X., Mitchell, R. N., Spencer, C. J., Ernst, R., Pisarevsky, S., Kirscher, U. & Murphy, J. B. 2019. Decoding  
 722 Earth's rhythms: Modulation of supercontinent cycles by longer superocean episodes. *Precambrian Research* 323,  
 723 1-5.
- 724 Lin, S., Xing, G., Davis, D. W., Yin, C., Wu, M., Li, L., Jiang, Y. & Chen, Z. 2018. Appalachian-style multi-terrace  
 725 Wilson cycle model for the assembly of South China. *Geology* 46, 319-322.
- 726 Lin, W., Monié, P., Faure, M., Schärer, U., Shi, Y., Breton, N. L. & Wang, Q. 2011. Cooling paths of the NE China  
 727 crust during the Mesozoic extensional tectonics: Example from the south-Liaodong peninsula metamorphic core  
 728 complex. *Journal of Asian Earth Sciences* 42, 1048-1065.
- 729 Liu, F., Liu, P., Wang, F., Liu, J., Meng, E., Cai, J. & Shi, J. 2014. U–Pb dating of zircons from granitic leucosomes  
 730 in migmatites of the Jiaobei Terrane, southwestern Jiao–Liao–Ji Belt, North China Craton: Constraints on the  
 731 timing and nature of partial melting. *Precambrian Research* 245, 80-99.
- 732 Liu, F. L., Gerdes, A., Liou, J. G., Xue, H. M. & Liang, F. H. 2006. SHRIMP U-Pb zircon dating from Sulu-Dabie  
 733 dolomitic marble, eastern China: constraints on prograde, ultrahigh-pressure and retrograde metamorphic ages.  
 734 *Journal of Metamorphic Geology* 24, 569-589.
- 735 Liu, L., Liu, F., Guo, J., Liu, P., Wang, W. & Cai, J. 2021. Geochronological and geochemical constraints on the non-  
 736 ultrahigh-pressure metasedimentary blocks of North China affinity within the Sulu ultrahigh-pressure belt, eastern  
 737 China, and tectonic implications. *International Geology Review*, DOI: 10.1080/00206814.00202021.01882889.
- 738 Liu, L., Liu, F., Santosh, M., Wang, H. & Ji, L. 2018. Paleoproterozoic and Triassic metamorphic events in the  
 739 Jiaobei Terrane, Jiao-Liao-Ji Belt, China: Hidden clues on multiple metamorphism and new insights into complex  
 740 tectonic evolution. *Gondwana Research* 60, 105-128.
- 741 Liu, P., Liu, F., Yang, H., Wang, F. & Liu, J. 2012. Protolith ages and timing of peak and retrograde metamorphism  
 742 of the high-pressure granulites in the Shandong Peninsula, eastern North China Craton. *Geoscience Frontiers* 3,  
 743 923-943.
- 744 Liu, X. C., Jahn, B. M., Hu, J., Li, S. Z., Liu, X. & Song, B. 2011. Metamorphic patterns and SHRIMP zircon ages  
 745 of medium-to-high grade rocks from the Tongbai orogen, central China: implications for multiple  
 746 accretion/collision processes prior to terminal continental collision. *Journal of Metamorphic Geology* 29, 979-  
 747 1002.
- 748 Mao, J., Ye, H., Liu, K., Li, Z., Takahashi, Y., Zhao, X. & Kee, W.-S. 2013. The Indosinian collision–extension event  
 749 between the South China Block and the Palaeo-Pacific plate: Evidence from Indosinian alkaline granitic rocks in  
 750 Dashuang, eastern Zhejiang, South China. *Lithos* 172-173, 81-97.
- 751 Meng, L. & Lin, W. 2021. Late Triassic contractional tectonics in the overriding plate of the Sulu orogenic belt,  
 752 Eastern China. *Tectonophysics* 806, DOI: 10.1016/j.tecto.2021.228793.
- 753 Meng, Q. R. & Zhang, G. W. 1999. Timing of collision of the North and South China blocks: Controversy and  
 754 reconciliation. *Geology* 27, 123-126.
- 755 Metcalfe, I. 1998. Palaeozoic and Mesozoic geological evolution of the SE Asian region: multidisciplinary  
 756 constraints and implications for biogeography. *Biogeography and Geological Evolution of SE Asian*, 25-41.
- 757 Metcalfe, I. 2006. Palaeozoic and Mesozoic tectonic evolution and palaeogeography of East Asian crustal fragments:  
 758 The Korean Peninsula in context. *Gondwana Research* 9, 24-46.

- 759 Metcalfe, I. 2013. Gondwana dispersion and Asian accretion: Tectonic and palaeogeographic evolution of eastern  
760 Tethys. *Journal of Asian Earth Sciences* **66**, 1-33.
- 761 Meinhold, G. 2010. Rutile and Its Application in Earth Sciences. *Earth-Science Reviews* **102**, 1-28.
- 762 Nam, T. N., Sano, Y., Terada, K., Toriumi, M., Van Quynh, P. & Dung, L. T. 2001. First SHRIMP U-Pb zircon dating  
763 of granulites from the Kontum massif Vietnam and tectonothermal implications. *Journal of Asian Earth Sciences*  
764 **19**, 77-84.
- 765 Oh, C. W. 2015. The Continental Collision Process Deduced from the Metamorphic Pattern in the Dabie-Hongseong  
766 and Himalayan Collision Belts. *Subduction Dynamics: From Mantle Flow to Mega Disasters* **211**, 19.
- 767 Okay, A. I., Xu, S. & Sengor, A. C. 1989. Coesite from the Dabie Shan eclogites, central China. *European Journal of*  
768 *Mineralogy* **1**, 595-598.
- 769 Qiu, Y. M., Gao, S., McNaughton, N. J., Groves, D. I. & Ling, W. 2000. First evidence of > 3.2 Ga continental crust  
770 in the Yangtze craton of south China and its implications for Archean crustal evolution and Phanerozoic tectonics.  
771 *Geology* **28**, 11-14.
- 772 Roberts, M. P. & Finger, F. 1997. Do U-Pb zircon ages from granulites reflect peak metamorphic conditions?  
773 *Geology* **25**, 319-322.
- 774 Roger, F., Maluski, H., Leyreloup, A., Lepvrier, C. & Truong Thi, P. 2007. U-Pb dating of high temperature  
775 metamorphic episodes in the Kon Tum Massif Vietnam. *Journal of Asian Earth Sciences* **30**, 565-572.
- 776 Rowley, D. B., Ziegler, A. M., Gyou, N., Hsü, K. J., Shu, S., Jiliang, L., Haihong, C., Haipo, P. & Sengor, A. 1989.  
777 Comment and Reply on " Mesozoic overthrust tectonics in south China". *Geology* **17**, 384-387.
- 778 Schmädicke, E., Will, T. M., Ling, X., Li, X.-H. & Li, Q.-L. 2018. Rare peak and ubiquitous post-peak zircon in  
779 eclogite: Constraints for the timing of UHP and HP metamorphism in Erzgebirge, Germany. *Lithos* **322**, 250-267.
- 780 Scotese, C. 1997. Paleogeographic Atlas, Paleomap progress report 90-0497. *University of Texas at Arlington*.  
781 Arlington: <http://scotese.com/>.
- 782 Şengör, A. M. C. & Atayman, S. 2009. The Permian extinction and the Tethys: an exercise in global geology. *The*  
783 *Geological Society of America, USA*, doi.org/10.1130/SPE1448.
- 784 Shen, J., Chen, J., Algeo, T. J., Yuan, S., Feng, Q., Yu, J., Zhou, L., O'Connell, B. & Planavsky, N. J. 2019. Evidence  
785 for a prolonged Permian-Triassic extinction interval from global marine mercury records. *Nat Commun* **10**, 1563.
- 786 Shen, L., Yu, J.-H., O'Reilly, S. Y., Griffin, W. L. & Wang, Q. 2016. Widespread Paleoproterozoic basement in the  
787 eastern Cathaysia Block: Evidence from metasedimentary rocks of the Pingtan–Dongshan metamorphic belt, in  
788 southeastern China. *Precambrian Research* **285**, 91-108.
- 789 Shen, Y., Farquhar, J., Zhang, H., Masterson, A., Zhang, T. & Wing, B. A. 2011. Multiple S-isotopic evidence for  
790 episodic shoaling of anoxic water during Late Permian mass extinction. *Nat Commun* **2**, 210.
- 791 Shu, L., Faure, M., Wang, B., Zhou, X. & Song, B. 2008. Late Palaeozoic-Early Mesozoic geological features of  
792 south China: Response to the Indosinian collision events in southeast Asia. *Comptes Rendus Geosciences* **340**,  
793 151-165.
- 794 Shu, L. S., Jahn, B. M., Charvet, J., Santosh, M., Wang, B., Xu, X. S. & Jiang, S. Y. 2014. Early Paleozoic  
795 depositional environment and intraplate tectono-magmatism in the Cathaysia Block South China: Evidence from  
796 stratigraphic, structural, geochemical and geochronological investigations. *American Journal of Science* **314**, 154-  
797 186.
- 798 Sláma, J., Košler, J., Condon, D. J., Crowley, J. L., Gerdes, A., Hanchar, J. M., Horstwood, M. S. A., Morris, G. A.,  
799 Nasdala, L., Norberg, N., Schaltegger, U., Schoene, B., Tubrett, M. N., and Whitehouse, M. J., 2008. Plešovice  
800 zircon — A new natural reference material for U–Pb and Hf isotopic microanalysis. *Chemical Geology* **249**, 1-  
801 35.
- 802 Song, M., Shu, L., Santosh, M. & Li, J. 2015. Late Early Paleozoic and Early Mesozoic intracontinental orogeny in  
803 the South China Craton: Geochronological and geochemical evidence. *Lithos* **232**, 360-374.
- 804 Spencer, K. J., Hacker, B. R., Kylander-Clark, A. R. C., Andersen, T. B., Cottle, J. M., Stearns, M. A., Poletti, J. E.,  
805 and Seward, G. G. E., 2013. Campaign-style titanite U–Pb dating by laser-ablation ICP: Implications for crustal  
806 flow, phase transformations and titanite closure. *Chemical Geology* **341**, 84-101.
- 807 Stampfli, G. M., Hochard, C., Vèrard, C., Wilhem, C. & vonRaumer, J. 2013. The formation of Pangea.  
808 *Tectonophysics* **593**, 1-19.
- 809 Torsvik, T. H. & Cocks, R. M. 2016. Earth history and Paleogeography. *Cambridge University Press*,  
810 doi.org/10.1017/9781316225523.
- 811 Viglietti, P. A., Benson, R. B. J., Smith, R. M. H., Botha, J., Kammerer, C. F., Skosan, Z., Butler, E., Crean, A.,  
812 Eloff, B., Kaal, S., Mohoi, J., Molehe, W., Mtalana, N., Mtungata, S., Ntheri, N., Ntsala, T., Nyaphuli, J., October,  
813 P., Skinner, G., Strong, M., Stummer, H., Wolvaardt, F. P. & Angielczyk, K. D. 2021. Evidence from South Africa  
814 for a protracted end-Permian extinction on land. *Proc Natl Acad Sci U S A* **118**.

- 815 Wang, L., Kusky, T. M., Polat, A., Wang, S., Jiang, X., Zong, K., Wang, J., Deng, H. & Fu, J. 2014. Partial melting  
816 of deeply subducted eclogite from the Sulu orogen in China. *Nat Commun* **5**, 5604.
- 817 Wang, W., Zhou, M.-F., Yan, D.-P., Li, L. & Malpas, J. 2013a. Detrital zircon record of Neoproterozoic active-  
818 margin sedimentation in the eastern Jiangnan Orogen, South China. *Precambrian Research* **235**, 1-19.
- 819 Wang, X. & Liou, J. 1991. Regional ultrahigh-pressure coesite-bearing eclogitic terrane in central China: Evidence  
820 from country rocks, gneiss, marble, and metapelite. *Geology* **19**, 933-936.
- 821 Wang, X., Liou, J. & Mao, H. 1989. Coesite-bearing eclogite from the Dabie Mountains in central China. *Geology*  
822 **17**, 1085-1088.
- 823 Wang, Y.-F., Li, X.-H., Jin, W. & Zhang, J.-H. 2015. Eoarchean ultra-depleted mantle domains inferred from ca.  
824 3.81Ga Anshan trondhjemitic gneisses, North China Craton. *Precambrian Research* **263**, 88-107.
- 825 Wang, Y., Fan, W., Zhang, G. & Zhang, Y. 2013b. Phanerozoic tectonics of the South China Block: Key observations  
826 and controversies. *Gondwana Research* **23**, 1273-1305.
- 827 Wang, Y., Wang, Y., Zhang, Y., Cawood, P. A., Qian, X., Gan, C., Zhang, F. & Zhang, P. 2021. Triassic two-stage  
828 intra-continental orogenesis of the South China Block, driven by Paleotethyan closure and interactions with  
829 adjoining blocks. *Journal of Asian Earth Sciences* **206**.
- 830 Wang, Y., Wu, C., Zhang, A., Fan, W., Zhang, Y., Zhang, Y., Peng, T. & Yin, C. 2012. Kwangsi and Indosinian  
831 reworking of the eastern South China Block: Constraints on zircon U–Pb geochronology and metamorphism of  
832 amphibolites and granulites. *Lithos* **150**, 227-242.
- 833 Wang, Z., Deng, Q., Duan, T., Yang, F., Du, Q., Xiong, X., Liu, H. & Cao, B. 2018. 2.85 Ga and 2.73 Ga A-type  
834 granites and 2.75 Ga trondhjemite from the Zhongxiang Terrain: Implications for early crustal evolution of the  
835 Yangtze Craton, South China. *Gondwana Research* **61**, 1-19.
- 836 Williams, I.S., 1998. U-Th-Pb geochronology by ion microprobe. In: Mckibben, M.A., Shanks, W.C., Ridley, W.I.  
837 Eds, Applications of Microanalytical Techniques to Understanding Mineralizing Processes 7. *Rev. Geol.* 1-35.
- 838 Winguth, C. & Winguth, A. M. E. 2012. Simulating Permian–Triassic oceanic anoxia distribution: Implications for  
839 species extinction and recovery. *Geology* **40**, 127-130.
- 840 Wu, F.-Y., Yang, J.-H., Xu, Y.-G., Wilde, S. A. & Walker, R. J. 2019. Destruction of the North China Craton in the  
841 Mesozoic. *Annual Review of Earth and Planetary Sciences* **47**, 173-195.
- 842 Wu, F. Y., Wan, B., Zhao, L., Xiao, W. J. & Zhu, R. X. 2020. Tethyan geodynamics. *Acta Petrologica Sinica* **36**,  
843 1627-1674 In Chinese with English abstract.
- 844 Wu, M., Zhao, G., Sun, M., Li, S., Bao, Z., Tam, P. Y., Eizenhöfer, P. R. & He, Y. 2014. Zircon U–Pb  
845 geochronology and Hf isotopes of major lithologies from the Jiaodong Terrane: Implications for the crustal  
846 evolution of the Eastern Block of the North China Craton. *Lithos* **190-191**, 71-84.
- 847 Wu, S., Karius, V., Schmidt, B. C., Simon, K., and Worner, G., 2018, Comparison of Ultrafine Powder Pellet and  
848 Flux-free Fusion Glass for Bulk Analysis of Granitoids by Laser Ablation-Inductively Coupled Plasma-Mass  
849 Spectrometry. *Geostandards and Geoanalytical Research* **42**, 575-591.
- 850 Wu, Y.-B. & Zheng, Y.-F. 2013. Tectonic evolution of a composite collision orogen: An overview on the Qinling–  
851 Tongbai–Hong’an–Dabie–Sulu orogenic belt in central China. *Gondwana Research* **23**, 1402-1428.
- 852 Wu, Y. 2009. Multistage evolution of continental collision orogen: A case study for western Dabie orogen. *Chinese*  
853 *Science Bulletin* **54**, 2568-2579.
- 854 Wu, Y. B., Zheng, Y. F., Tang, J., Gong, B., Zhao, Z. F. & Liu, X. 2007. Zircon U-Pb dating of water-rock interaction  
855 during Neoproterozoic rift magmatism in South China. *Chemical Geology* **246**, 65-86.
- 856 Xia, Y. & Xu, X. 2019. A Fragment of Columbia Supercontinent: Insight for Cathaysia Block Basement From  
857 Tectono-Magmatic Evolution and Mantle Heterogeneity. *Geophysical Research Letters* **46**, 2012-2024.
- 858 Xia, Y. & Xu, X. 2020. The epilogue of Paleo-Tethyan tectonics in the South China Block: Insights from the Triassic  
859 aluminous A-type granitic and bimodal magmatism. *Journal of Asian Earth Sciences* **190**.
- 860 Xiao, W. & He, H. 2005. Early Mesozoic thrust tectonics of the northwest Zhejiang region Southeast China.  
861 *Geological Society of America Bulletin* **117**, 945-961.
- 862 Xu, S., Ai, O., Ji, S., AMC, S., Su, W., Liu, Y. & Jiang, L. 1992. Diamond from the Dabie Shan metamorphic rocks  
863 and its implication for tectonic setting. *Science* **256**, 80-82.
- 864 Yang, J.-H., Wu, F.-Y., Wilde, S. A., Belousova, E. & Griffin, W. L. 2008. Mesozoic decratonization of the North  
865 China block. *Geology* **36**, 467-470.
- 866 Ye, H., Wu, C.-Z., Yang, T., Santosh, M., Yao, X.-Z., Gao, B.-F., Wang, X.-L. & Li, W. 2017. Updating the Geologic  
867 Barcodes for South China: Discovery of Late Archean Banded Iron Formations in the Yangtze Craton. *Scientific*  
868 *Reports* **7**.
- 869 Ye, K., Cong, B. & Ye, D. 2000. The possible subduction of continental material to depths greater than 200km.  
870 *Nature* **407**, 734-736.

- 871 Yin, A. & Nie, S. 1993. An indentation model for the North and South China collision and the development of the  
872 Tan-Lu and Honam fault systems, eastern Asia. *Tectonics* **12**, 801-813.
- 873 Yin, H., Jiang, H., Xia, W., Feng, Q., Zhang, N. & Shen, J. 2014. The end-Permian regression in South China and its  
874 implication on mass extinction. *Earth-Science Reviews* **137**, 19-33.
- 875 Yin, H., Xie, S., Luo, G., Algeo, T. J. & Zhang, K. 2012. Two episodes of environmental change at the Permian–  
876 Triassic boundary of the GSSP section Meishan. *Earth-Science Reviews* **115**, 163-172.
- 877 Yu, J., Zhou, X., O'Reilly, Y., Zhao, L., Griffin, W., Wang, R., Wang, L. & Chen, X. 2005. Formation history and  
878 protolith characteristics of granulite facies metamorphic rock in Central Cathaysia deduced from U-Pb and Lu-Hf  
879 isotopic studies of single zircon grains. *Chinese Science Bulletin* **50**, 2080-2089.
- 880 Yu, J., Zhou, X., Zhao, L. & Chen, X. 2003. Discovery and implications of granulite facies metamorphic rocks in the  
881 eastern Nanling, China. *Acta Petrologica Sinica* **19**, 461-467 In Chinese with English abstract.
- 882 Zhai, M. 2011. Cratonization and the Ancient North China Continent: A summary and review. *Science China Earth  
883 Sciences* **54**, 1110-1120.
- 884 Zhai, M. 2014. Multi-stage crustal growth and cratonization of the North China Craton. *Geoscience Frontiers* **5**,  
885 457-469.
- 886 Zhang, A., Ma, L., Liu, H., Cai, Y., Chen, M. & Fang, Q. 2021a. Identification of two-phased late Paleoproterozoic  
887 magmatism in the Wuyishan Domain SE China: Implications for the tectonic evolution of the Cathaysia Block.  
888 *Precambrian Research* **355**, 106093.
- 889 Zhang, G., Guo, A., Wang, Y., Li, S., Dong, Y., Liu, S., He, D., Cheng, S., Lu, R. & Yao, A. 2013a. Tectonics of  
890 South China continent and its implications. *Science China Earth Sciences* **56**, 1804-1828.
- 891 Zhang, G. W., Cheng, S. Y., Guo, A., Dong, Y. P., Lai, S. & Yao, Y. P. 2004. Mianlue paleo-suture on the southern  
892 margin of the Central Orogenic System in Qinling-Dabie - with a discussion of the assembly of the main part of the  
893 continent China. *Geological Bulletin of China* **23**, 846-853 In Chinese with English abstract.
- 894 Zhang, H., Zhang, F., Chen, J.-B., Erwin, D. H., Syverson, D. D., Ni, P., Rampino, M., Chi, Z., Cai, Y.-f., Xiang, L.,  
895 Li, W.-Q., Liu, S.-A., Wang, R.-C., Wang, X.-d., Feng, Z., Li, H.-m., Zhang, T., Cai, H.-m., Zheng, W., Cui, Y.,  
896 Zhu, X.-k., Hou, Z.-q., Wu, F.-y., Xu, Y.-g., Planavsky, N. & Shen, S.-z. 2021b. Felsic volcanism as a factor  
897 driving the end-Permian mass extinction. *Science Advances* **7**, eabh1390.
- 898 Zhang, J., Qu, J., Zhang, B., Zhao, H., Wang, Y. & Lu, M. 2017. Paleozoic to Mesozoic deformation of eastern  
899 Cathaysia: A case study of the Chencai complex, Zhejiang Province, eastern China, and its tectonic implications.  
900 *GSA Bulletin*, <https://doi.org/10.1130/B31680.31681>.
- 901 Zhang, R., Lo, C., Chung, S., Grove, M., Omori, S., Iizuka, T., Liou, J. & Tri, T. V. 2013b. Origin and tectonic  
902 implication of Ophiolite and eclogite in the Song Ma Suture Zone between the South China and Indochina Block.  
903 *Journal of Metamorphic Geology* **31**.
- 904 Zhang, R. Y., Lo, C., Li, X. H., Chung, S., Anh, T. T. & Tri, T. V. 2014a. U-Pb dating and tectonic implication of  
905 ophiolite and metabasite from the Song Ma Suture zone, Northern Vietnam. *American Journal of Science* **314**.
- 906 Zhang, S.-B., Zheng, Y.-F., Wu, Y.-B., Zhao, Z.-F., Gao, S. & Wu, F.-Y. 2006. Zircon isotope evidence for  $\geq 3.5$ Ga  
907 continental crust in the Yangtze craton of China. *Precambrian Research* **146**, 16-34.
- 908 Zhang, S.-H., Zhao, Y., Davis, G. A., Ye, H. & Wu, F. 2014b. Temporal and spatial variations of Mesozoic  
909 magmatism and deformation in the North China Craton: Implications for lithospheric thinning and  
910 decratonization. *Earth-Science Reviews* **131**, 49-87.
- 911 Zhao, G. & Zhai, M. 2013. Lithotectonic elements of Precambrian basement in the North China Craton: Review and  
912 tectonic implications. *Gondwana Research* **23**, 1207-1240.
- 913 Zhao, L., Li, T., Peng, P., Guo, J., Wang, W., Wang, H., Santosh, M. & Zhai, M. 2015a. Anatomy of zircon growth in  
914 high pressure granulites: SIMS U–Pb geochronology and Lu–Hf isotopes from the Jiaobei Terrane, eastern North  
915 China Craton. *Gondwana Research* **28**, 1373-1390.
- 916 Zhao, L., Zhai, M., Santosh, M. & Zhou, X. 2017. Early Mesozoic retrograded eclogite and mafic granulite from the  
917 Badu Complex of the Cathaysia Block, South China: Petrology and tectonic implications. *Gondwana Research*  
918 **42**, 84-103.
- 919 Zhao, L., Zhai, M. & Zhou, X. 2022. Formation of an intracontinental orogen above the Permo-Triassic mantle  
920 convection cell in the Paleo-Tethys tectonic realm due to far-field stress derived from continental margins.  
921 *Frontiers in Earth Science*, DOI: 10.3389/feart.2022.892787.
- 922 Zhao, L., Zhai, M., Zhou, X., Santosh, M. & Ma, X. 2016. Thermal gradient and geochronology of a Paleozoic high-  
923 grade terrane in the northeastern Cathaysia block, South China. *Tectonophysics* **691**, 311-327.
- 924 Zhao, L., Zhou, X., Zhai, M., Liu, B. & Cui, X. 2018. Petrologic and zircon U–Pb geochronological characteristics  
925 of the pelitic granulites from the Badu Complex of the Cathaysia Block, South China. *Journal of Asian Earth  
926 Sciences* **158**, 65-79.

- 927 Zhao, L., Zhou, X., Zhai, M., Santosh, M. & Geng, Y. 2015b. Zircon U–Th–Pb–Hf isotopes of the basement rocks in  
928 northeastern Cathaysia block, South China: Implications for Phanerozoic multiple metamorphic reworking of a  
929 Paleoproterozoic terrane. *Gondwana Research* **28**, 246-261.
- 930 Zheng, Y. F., Zhou, J. B., Wu, Y. B. & Xie, Z. 2005. Low-grade metamorphic rocks in the Dabie-Sulu Orogenic Belt:  
931 a passive-margin accretionary wedge deformed during continent subduction. *International Geology Review* **47**,  
932 851-871.
- 933 Zhou, L.-G., Xia, Q.-X., Zheng, Y.-F. & Chen, R.-X. 2011. Multistage growth of garnet in ultrahigh-pressure  
934 eclogite during continental collision in the Dabie orogen: Constrained by trace elements and U–Pb ages. *Lithos*  
935 **127**, 101-127.
- 936 Zhou, L.-G., Xia, Q.-X., Zheng, Y.-F., Chen, R.-X., Hu, Z. & Yang, Y. 2015. Tectonic evolution from oceanic  
937 subduction to continental collision during the closure of Paleotethyan ocean: Geochronological and geochemical  
938 constraints from metamorphic rocks in the Hong'an orogen. *Gondwana Research* **28**, 348-370.
- 939 Zhu, G., Chen, Y., Jiang, D. & Lin, S. 2015. Rapid change from compression to extension in the North China Craton  
940 during the Early Cretaceous: Evidence from the Yunmengshan metamorphic core complex. *Tectonophysics* **656**,  
941 91-110.
- 942 Zhu, R.-X., Yang, J.-H. & Wu, F.-Y. 2012. Timing of destruction of the North China Craton. *Lithos* **149**, 51-60.  
943  
944